NO$_2$ vertical profiles and column densities from MAX-DOAS measurements in Mexico City

Martina Michaela Friedrich[1,2], Claudia Rivera[1,3], Wolfgang Stremme[1], Zuleica Ojeda[1], Josué Arellano[1], Alejandro Bezanilla[1], José Agustín García-Reynoso[1], and Michel Grutter[1]

[1]Centro de Ciencias de la Atmósfera, Universidad Nacional Autónoma de México
[2]Belgian Institute for Space Aeronomie (BIRA-IASB)
[3]Facultad de Química, Universidad Nacional Autónoma de México

Correspondence: M.M. Friedrich (martina@atmosfera.unam.mx)

Abstract. We present a new numerical code, Mexican Maxdoas Fit (MMF), developed to retrieve profiles of different trace gases from the network of MAX-DOAS instruments operated in Mexico City. MMF uses differential slant column densities (dSCDs) retrieved with the QDOAS (Danckaert et al., 2013) software. The retrieval is comprised of two steps, an aerosol retrieval and the trace gas retrieval that uses the retrieved aerosol profile in the forward model for the trace gas. For forward model simulations, VLIDORT is used (e.g. Spurr et al., 2001; Spurr, 2006, 2013). Both steps use constrained least square fitting, but the aerosol retrieval uses Tikhonov regularization and the trace gas retrieval optimal estimation. Aerosol optical depth and scattering properties from the AERONET database, averaged ceilometer data, WRF-Chem model data as well as temperature and pressure sounding data are used for different steps in the retrieval chain.

The MMF code was applied to retrieve NO$_2$ profiles with two degrees of freedom (DOF=2) from spectra of the MAX-DOAS instrument located at the UNAM campus. We describe the full error analysis of the retrievals and include a sensitivity exercise to quantify the contribution of the uncertainties in the aerosol extinction profiles to the total error. A dataset comprised of measurements from January 2015 to July 2016 was processed and the results compared to independent surface measurements. We concentrate on the analysis of 4 single days and additionally present diurnal and annual variabilities from averaging the 1.5 years of data. The total error, depending on the exact counting is 14 –20 % and this work provides new and relevant information about NO$_2$ in the boundary layer of Mexico City

1 Introduction

Air pollution is a serious environmental problem due to its negative impacts on human health and ecosystems. Fast growing urban and industrial centers are continuously affected by bad air quality and in order to assess their current efforts to mitigate emissions and plan for more efficient strategies to lower the concentration levels of harmful contaminants, it is indispensable to have the proper tools to measure them not only at ground level but also throughout the boundary layer (García-Franco et al., 2018). The Multi-AXis Differential Optical Absorption Spectroscopy (MAX-DOAS) technique (e.g. Hönninger et al., 2004; Platt and Stutz, 2008) has rapidly developed in recent years and has proven extremely valuable in tropospheric chemistry and air pollution studies, since it provides vertical distribution of trace gases with high temporal resolution.

This remote sensing technique is based on the spectroscopically resolved measurement of scattered sunlight at different elevation angles, allowing for the retrieval of total column amounts of aerosols and trace gases with profiling capability. Powerful applications of this technique have been demonstrated to provide useful information about the vertical distribution of aerosols (Frieß et al., 2006; Wang et al., 2016) and photochemically relevant species such as nitrogen dioxide (NO_2),

5   formaldehyde (HCHO), glyoxal (CHOCHO) and nitrous acid (HONO) among other gases (e.g. Wittrock et al., 2004; Wagner et al., 2011; Ortega et al., 2015; Hendrick et al., 2014).

Photochemical reactions involving NO_2 play an important role in the formation of O_3 (Finlayson-Pitts and Pitts, 2000). The Mexico City Metropolitan Area (MCMA) has been particularly affected since the 1990's by high O_3 episodes threatening the population and forcing the authorities to impose strict restrictions on the usage of motor vehicles (Molina and Molina, 2002).

10   Measurements have been performed in the region using fixed and mobile DOAS zenith-scattered sunlight (Melamed et al., 2009; Johansson et al., 2009; Rivera et al., 2013). In 2014, a MAX-DOAS network, initially consisting of four instruments, was established in the Mexico City Metropolitan Area (MCMA) which has been operating since (Arellano et al., 2016).

In this contribution, we describe the MMF (Mexican Maxdoas Fit) code that has been implemented to retrieve vertical distribution of aerosols and trace gases with emphasis on the errors and diagnostics of the results. An overview of the MAX-

15   DOAS instruments is provided in Sect. 2 and the complete retrieval strategy from the measured spectra to vertical trace gas profiles is summarized in Fig. 1.

Radiative transfer simulations (constituting the forward model in MMF, yellow boxes in Fig. 1) are performed with VLI-DORT (Spurr, 2013) to derive simulated differential slant column densities (dSCDs) at the middle of the corresponding wavelength interval used to derive dSCDs from measured spectra. The dSCD retrieval (blue boxes in Fig. 1) is performed with

20   QDOAS (Danckaert et al., 2013) and is described briefly in Sect. 3. The orange parts in the figure refer to the aerosol retrieval while the green parts belong to the trace gas retrieval. Details on the forward model choice, the forward model input calculation (light blue box in Fig. 1) and processing of output quantities in the inversion algorithm are described in Sect. 4.

An error analysis has been included in Sect. 5, especially investigating the effect of the aerosol retrieval on the NO_2 results. Some examples of the NO_2 variability are provided from one of the network's stations and compared to surface concentrations

25   in Sect. 6 and a summary of the work and an outlook on planned improvements to the retrieval code is presented in Sect. 7.

2   Instruments

An instrument based on the MAX-DOAS technique was designed and developed by the Center for Atmospheric Sciences at the Universidad Nacional Autónoma de México (UNAM). It consists of two main parts: the scanner unit which collects the scattered light, and the acquisition/control unit, containing a spectrometer and computer that records and stores the measure-

30   ments. The two components are connected by an optical fiber and a data connection cable. Both are described briefly in the following sections. For a more complete description and a map of the area with the station locations and their measurement orientation, we refer the reader to Arellano et al. (2016).
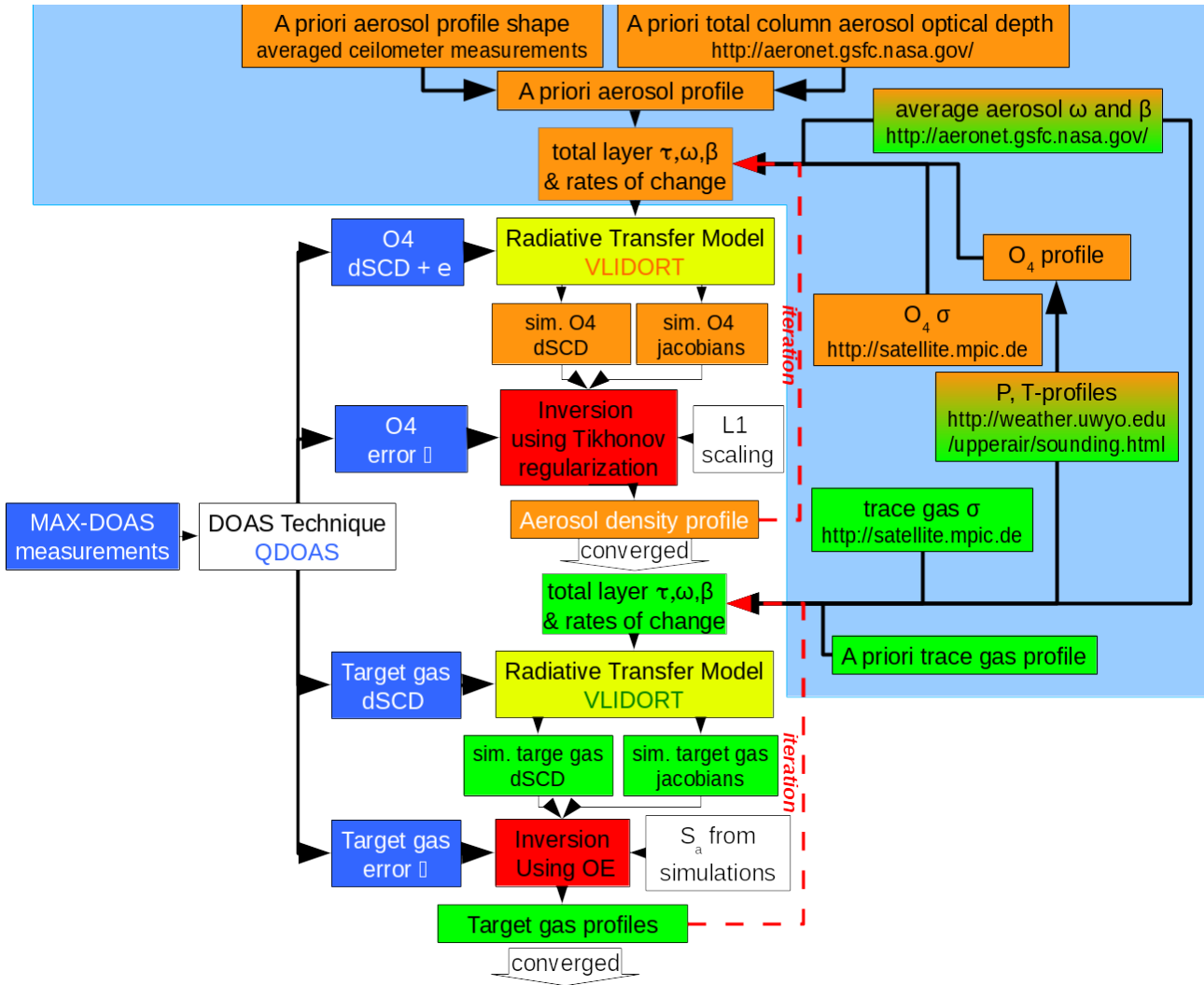
Figure 1. Flowchart of the complete trace gas retrieval algorithm. Orange boxes belong to the aerosol retrieval, green boxes to trace gas retrieval. The light blue box encompasses forward-model-input calculation. The dark blue boxes are in/ outputs of QDOAS. The yellow boxes represent the forward modelling steps. The red boxes are the inversion steps, using Tikhonov regularization for aerosol retrieval and optical estimation (OE) for tracegas retrieval.

2.1 The scanner

The scanner is composed of a plastic enclosure (NEMA-rated type 3) resistant to sunlight and hermetically sealed to protect the inner parts from water and bugs. This is important in order to assure long measurement periods under harsh conditions (Hönninger et al., 2004; Galle et al., 2010; Arellano et al., 2016). The scattered light is collected by a plano-convex quartz lens (Edmund Optics, $\oslash$ = 25.4 mm, f = 100 mm), focusing it into the entrance of an optical fiber (Fiber Tech Optica, quartz, 6 m long, $\oslash$ = 0.6 mm) which transfers the light into the acquisition/control unit. These optical parts are mounted inside a telescope housing constructed of Nylamid material. A shutter system is installed also within the telescope. It consists of a stepper motor (Mercury, $7.5°$ by step) that rotates a metal circular plate to prevent the passage of light into the optical fiber and an optical switch which is used to indicate the position of the plate. The shutter is used to make measurements of dark spectra in between scans.

A stepper motor (Oriental Motors, PK266-02A) inside the enclosure allows the movement of the scanner unit in a range of $180°$ with steps of $0.1°$. A mechanical switch is used as a reference to indicate the starting position of each scan. The motor is controlled by an electronic board composed of an 8-bit microcontroller (AVR- architecture), a RS-232 port for communication with the acquisition/control unit, a temperature sensor (Maxim 18B20, accuracy $\pm0.5°$C), and a dual axis accelerometer (Analog Devices, accuracy $\pm0.1°$) that provides an accurate determination of the telescope's pointing elevation. The theoretical field of view (FOV) of the optical system is $0.31°$.

2.2 The acquisition/control unit

The second part of the instrument consists of a metallic housing receiving the collected light through the optical fiber and sending it to the spectrometer (Ocean Optics, USB2000+). This commercial device has a crossed asymmetric Czerny-Turner configuration, diffraction grating (1800 lines/mm) and a slit size of 50 μm wide x 1 mm high, recording spectra in a wavelength range of 289 - 510 nm at a resolution of 0.69 nm (full width at half maximum). It uses a Charge-Coupled Device (CCD) detector array (Sony ILX511B) of 2048 pixels with an integration time adjustable between 1 ms to 65 s.

Because changes in temperature can affect the wavelength/pixel ratio and also modify the optical properties of the spectrometer like the alignment and the line shape (e.g. Carlson et al., 2010; Coburn et al., 2011), a temperature control system composed of a Peltier cell (Multicomp) and three temperature sensors (Maxim 18B20, accuracy $\pm0.5°$C) controlled by an electronic board were implemented. The cooling side of the Peltier cell was placed on top of the spectrometer and the heating side was attached to a heat sink. The Peltier cell and the spectrometer were wrapped in a styrofoam box to keep the temperature insulated from the outside. The three temperature sensors were placed on the heat sink, the Peltier cell and spectrometer to monitor temperature changes. The temperature control system was wrapped in an aluminum enclosure to prevent the heat spreading to other parts of the system and a fan was installed to extract the heat from the enclosure.

The electronic board for the temperature control is composed of an 8-bit microcontroller (AVR, architecture) and a RS-232 communication port. This board is responsible for obtaining the data from the sensors and adjusting the voltage in the Peltier cell to keep the temperature constant.

The acquisition/ control unit has a laptop computer (Dell, Latitude 2021) with Linux operating system contained within the enclosure. The program controlling the hardware is written in C++ using Qt libraries. A script is used to carry out the measurement sequence previously defined and to monitor the spectrometer temperature.

2.3 Measurement strategy

A complete scan consists of a sequence that begins with a measurement towards the zenith, (90 ° elevation angle), followed by tree measurements between elevation angles 0 ° and 10 ° towards the west (for UNAM station, this is 85 ° azimuth angle), then 12 measurements are taken with elevation angles between 10 ° elevation angle towards west and 10 ° elevation angle towards the east (crossing the zenith, but without taking a measurement), followed by three measurements between 10 ° and 0 ° elevation angle towards the east. The same sequence is then repeated but in reverse order. At the end of this cycle, a dark spectrum with the closed shutter is taken. With this setup, a complete scan takes about 7 minutes. The measurement sequence (90°Zenith, 0°W, 2°W, 6°W, 13°W, 23°W, 36°W, 50°W, 65°W, 82°W, 82°E, 65°E, 50°E, 36°E, 23°E, 13°E, 6°E, 2°E, 0°E) is likely to change in the future to use longer integration times but at the same time reduce the number of viewing directions in the range between 10 ° elevation angle towards the west and 10 ° elevation angle towards the east in order to keep the total scan time roughly constant. All data presented in this manuscript uses this setup, meaning that we include both westerly and easterly viewing directions in the same retrieval and hence the result represents an average. This strategy leads to larger fitting errors since this likely deviates further from the assumption of horizontal homogeneity. With our retrieval chain, it is possible to consider the easterly and westerly directions separately to investigate the differences in viewing directions which is subject of current investigation.

The output from the MAX-DOAS instruments consists of five files per complete scan: A file containing the meta data of each spectrum (e.g. accelerometer data for each measurement, time of the acquisition, temperatures within the acquisition unit), all the spectra in non-zenith directions, the dark spectrum measured with the shutter closed, a meta file for the dark spectrum and the first zenith reference measurement. These files are stored for further processing.

3 Differential Slant Column Densities (dSCDs) Retrieval

The spectra were evaluated using the QDOAS (version 2.105) software (Danckaert et al., 2013). As a pre-processing step before the QDOAS analysis, the dark signal was subtracted from each of the measurement spectra. A wavelength calibration was conducted in QDOAS by applying a non-linear least squares fit to a solar atlas (Kurucz et al., 1984).

For NO_2, the retrieval was conducted in the 405 to 465 nm wavelength range using the spectrum measured at the zenith position at the beginning of each of the measurement sequences as reference. Using a single zenith reference before the scan (both for NO_2 and O_4) instead of a linear interpolation of zenith measurements before and after the scan, makes correct measurements during twilight problematic: since upper atmospheric contributions to the slant column density change rapidly during twilight, stratospheric NO2 could falsely be attributed to the troposphere. Hence, in the study presented here, no twilight measurements are included. For the analysis, differential cross-sections of NO_2 at 298 K (Vandaele et al., 1998), O_3 at 221 K
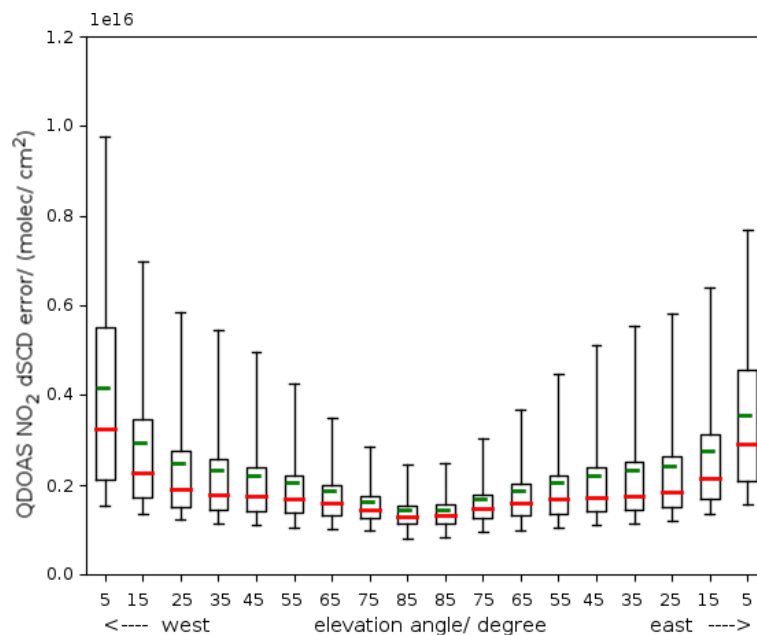
Figure 2. dSCDs measurement error statistics for NO_2 at the UNAM station as a function of elevation angle for data taken in the year 2016. The box encloses the 25-75 percentile, the whiskers are 5-95 percent, the green bar is the mean and the red bar the median.

and 241 K (Burrows et al., 1999) and the oxygen dimer (Hermans et al., 1999) were convolved with the slit function of the spectrometer and a wavelength calibration file (created using a mercury lamp) and using the convolution tool of the QDOAS software. A Ring spectrum, generated at 273 K from a high resolution Kurucz file using the Ring tool of the QDOAS software (Danckaert et al., 2013), was also included in the analysis.

5   For O_4, the retrieval was conducted in the 336 to 390 nm wavelength range. Differential cross-sections of O_4 (Hermans et al., 1999), O_3 at 221 K and 241 K (Burrows et al., 1999), NO_2 at 294 K (Vandaele et al., 1998), BrO at 298 K (Wilmouth et al., 1999), HCHO at 298 K (Meller and Moortgat, 2000) and a Ring spectrum were included in the analysis. A 3rd degree polynomial was used for the retrievals.

Fig. 2 shows the dSCDs retrieval error statistics for NO_2 as a function of elevation angle. The plot shows results of 31,448
10   scans from January to December 2016. Larger dSCDs fitting errors are found for viewing angles closer to the horizon (smaller elevation angles), likely due to physical interferences during the measurements. As elevation angles approach the zenith, retrieval dSCDs errors decrease considerably. The dSCD errors are the QDOAS calculated errors, a function of the fit residuals and the degree of freedom, see Danckaert et al. (2013) for details.

4 Mexican Maxdoas Fit

The method for the trace gas retrieval from slant column densities using the MMF code is comprised of two parts, an aerosol retrieval using the known O_4 profile, and the trace gas retrieval (e.g. Platt and Stutz, 2008). Both parts consist of the same steps: A foward model and an inversion algorithm.

In Sect.4.1, details about the inversion strategy are given. Our choice of forward model, VLIDORT (e.g. Spurr et al., 2001; Spurr, 2006, 2013), and the input parameter calculation are detailed in Section 4.2. How forward model output quantities are processed for the inversion step is detailed in Sect. 4.3.

The retrieval time per aerosol and trace gas retrieval with the Mexico City set-up is roughly half a minute for each scan, but highly dependent on the conditions.

4.1 Inversion theory

The inversion strategy relies on the fact that the problem is sufficiently linear so that in the iteration procedure, the new value for the quantity vector in question x (either the aerosol total extinction per layer or the trace gas optical depth per layer) can be calculated using a Gauss-Newton (GN) scheme[1] according to Eq. 1 (Rodgers, 2000). This step corresponds to the red box and arrows in Fig. 1.

$$x_{i+1} = x_a + (K_i^T S_m^{-1} K_i + R)^{-1} K_i^T S_m[(y - F(x_i)) - K_i(x_a - x_i)] \tag{1}$$

Here, superscript T denotes transposed, superscript -1 denotes the inverse. The index i is the iteration index, the subscript a indicates *a priori* values. S_m is the measurement error covariance matrix, y denotes the vector of measured differential slant column densities. $F(x_i)$ are the simulated differential slant column densities, calculated using the forward model with input profile x_i . Both y and $F(x_i)$ are vectors of dimension which is the number of telescope viewing angles. $K_i = \partial F(x)^l / \partial x_n$ is the Jacobian matrix at the i-th iteration describing the change of simulated dSCD for viewing angle l when the profile x in layer n is varied.

In the case of optimal estimation (OE), the regularization matrix R is equal to the inverse of the *a priori* covariance matrix, $R = S_a^{-1}$. OE regularization is used for trace gas retrieval. Other regularization matrices are possible, see e.g. Steck (2002).

For the aerosol retrieval used in this study, we use the $L1$ operator ($R = L1^T \alpha L1$) where the scaling parameter α is set to a constant value of 20 and is supplied via an input script to limit the degrees of freedom (DOF) to just slightly above 1. Different scalings for the upper layers and lower layers could be supplied, as well as a complete regularization matrix R.

4.2 Forward model

Several radiative transfer codes have been developed to serve as forward models for this kind of retrieval algorithms. For example, there are Monte Carlo (MC) codes, such as AMFTRAN (Marquard, 1998), TRACY (von Friedeburg et al., 2002;

---

[1]In a recent update, the GN scheme was replaced by the more stable Levenberg Marquardt (LM) iteration scheme, more details on recent changes can be found in Appendix A

von Friedeburg, 2003) or PROMSAR (Palazzi et al., 2005). All these MC radiative transfer codes start with ejecting photons from the instrument and following the photon path backwards (see also e.g. Perliski and Solomon, 1993; Marquard et al., 2000), hence they are sometimes somewhat confusingly referred to as backward models. The advantage of MC codes is their high accuracy, the disadvantage is the rather long calculation time. SCIATRAN (e.g. Buchwitz et al., 1998; Rozanov et al., 2014, 2017) combines multi scattering radiative transfer modelling using the Picard-Iterative approximation, a chemistry and an inversion code. It has been heavily used in NO_2 (e.g. Vidot et al., 2010) and ozone (e.g. Rahpoe et al., 2013b, a) retrieval from satellite observations.

Another class of radiative transfer codes, such as VLIDORT and DISORT (Stamnes et al., 1988; Dahlback and Stamnes, 1991), uses the discrete ordinate algorithm. This finite difference method is based on finding solutions for an atmosphere consisting of a number of homogeneous layers using gaussian quadrature approximations to the integro-differential radiative transfer equation expressed using Legendre polynomials for the phase function and Fourier series for the intensity.

The big advantage of the second class of codes is their high speed. Another advantage of VLIDORT is that it calculates not only the intensity but also analytic Jacobians. Therefore, instead of the $2 \times$ the number of layers calls to the program to perform a finite difference approximation, one call is sufficient. MMF uses the intensity part of VLIDORT, version 2.7, released in August 2014. (V)LIDORT is configured to return intensity Jacobians w.r.t. gas absorption layer properties or aerosol total extinction layer properties.

In MMF, the simulation grid is supplied via an input file to the code together with the corresponding *a priori* values of the trace gas concentration and the aerosol profile. The retrieval can be performed on the whole simulation grid or only on the lower part of the simulation grid. In this study, the simulation grid is identical to the retrieval grid and the layer distribution of the retrieval grid is not equidistant. The grid consists of 22 layers up to 25 km. The layer thickness increases from 100 m at the lowest layer to 5 km in the upper-most layer. The exact height distribution can be seen in Fig. 5. The surface albedo used in this study was set to 0.07, this value can be passed to MMF in the configuration file. However, in practice the effect for downwelling intensity and hence for the dSCD calculation was found to be negligible.

For each simulated atmospheric layer, the following input needs to be supplied to VLIDORT[2]:

1. total layer optical depth τ

2. single scattering albedo ω

3. phase function expansion coefficients β

Since Jacobians with respect to changes of quantity χ in each layer are required, the normalized derivatives of the total primary optical quantities, τ, ω and β with respect to this quantity need to be supplied as well. In case of trace gas retrieval, $\chi = a_{gas}\Delta h$, and in case of aerosol retrieval, $\chi = (\sigma_{aer} + a_{aer})\Delta h$. Here, a_{gas} and a_{aer} are the gaseous and aerosol absorption coefficients, respectively and σ_{aer} is the aerosol scattering coefficient. Δh is the layer thickness. Hence, for each layer the following input is additionally required:

---

[2]We only use the LIDORT part of VLIDORT, meaning that we only consider the total intensity and not the polarization
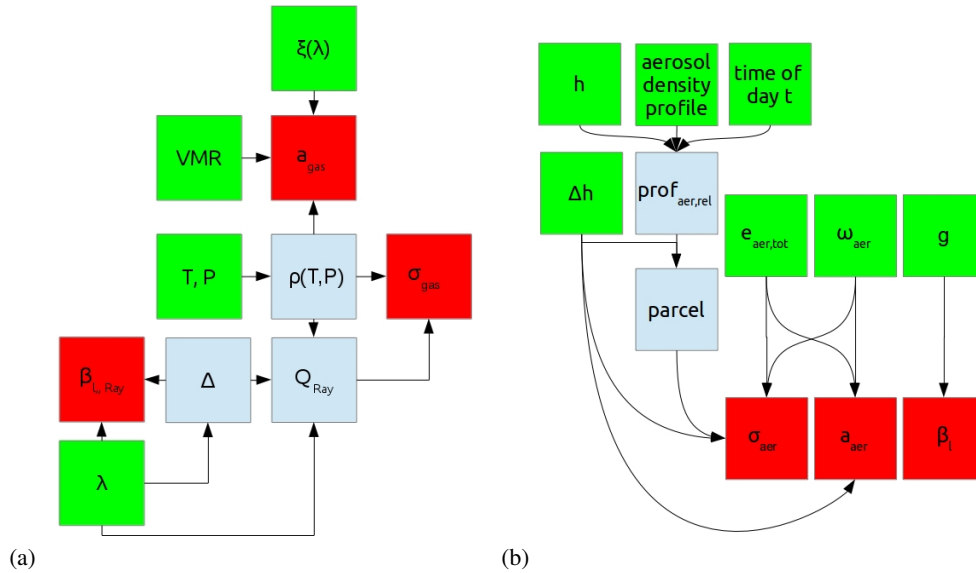
Figure 3. Calculating the gas and air (a) and aerosol (b) contribution to the layer input parameters for VLIDORT. The green boxes are primary input to MMF, blue boxes are intermediate quantities and red boxes final output that are combined for VLIDORT layer input. VMR denotes here the *a priori* volume mixing ratio. Instead of a VMR, an *a priori* trace gas density can be supplied, too.

4. normalized rate of change of τ w.r.t. χ

5. normalized rate of change of ω w.r.t. χ

6. normalized rate of change of β w.r.t. χ

In order to calculate this input, we first need to calculate the separate properties for the trace gases and the aerosols. After-
5 wards, these quantities are combined to yield the total layer quantities.

The calculation of the contribution from the trace gas and the air density (through Rayleigh scattering) for the layer inputs (1-6) is presented in Sect. 4.2.1. The aerosol contribution calculation is outlined in Sect. 4.2.2. These two sections also contain information on the source of information for the respective *a priori* values, as well as, for gas, the error covariance matrix.

The calculation of the contributions from gas and aerosol to yield the VLIDORT inputs (1-6) is detailed in Sect. 4.2.3.

10 **4.2.1 Input for gases**

In Fig. 3(a), the steps to calculate the contribution of the trace gas and the contribution from Rayleigh scattering in each layer are outlined. Red boxes represent the trace gas (and air) contribution to VLIDORT input quantities, green boxes are primary inputs to the inversion code, light blue boxes are intermediate quantities that are neither direct input to MMF, nor final input for the forward model.

The *a priori* volume mixing ratio (VMR) profile and the covariance matrix for this study are calculated from simulations covering the year 2011 using WRF-Chem V3.6. The model domain covers Mexico and surrounding seas, the domain has 200 by 100 square grid cells with approximately 28 km width and 35 vertical layers. The parameterizations used were for Micro Physics WRF single moment 3-class (4), for PBL the Yonsei University scheme (1), for Cumulus the Grell 3D ensemble scheme (5), for radiation the Goddard shortwave scheme (1) and the Dudhia long wave scheme (4), time-varying sea surface temperature on, grid analysis nudging on, the unified Noah Land Use surface model (2), off an urban canopy model and the 2008 emissions inventory were used.

MMF takes pressure and temperature profiles on a separate height grid, internal interpolation to the provided retrieval grid is performed. In the processing chain implemented in Mexico, the temperature and pressure profiles from radiosonde data for the specific day are downloaded from the University of Wyoming (http://weather.uwyo.edu/upperair/sounding.html) from the Mexico City Airport, station number 76679. These temperature and pressure profiles are linearly interpolated to the simulation grid used to calculate the dry air number density ρ, see Appendix B.

The absorption cross section ξ_λ is taken at a wavelength in the middle of the wavelength interval used for the QDOAS retrieval (see Sect. 3.), for aerosol retrieval it is 361 nm and for NO_2 it is 414 nm. The same cross-section tables as for QDOAS dSCD retrievals (see Sect. 3) are used for NO_2 and O_4. However, since the cross section cancels out at the end of the calculation, its exact value is not too important.

There are analytical fits to the temperature dependence, using e.g. linear (e.g. Vandaele et al., 2003, for NO_2) or more complicated (Kirmse et al., 1997, e.g.) temperature dependences. For a comparison study of different fitting functions, see Orphal (2002). These could be implemented, however, the cross-section is currently not temperature dependent, in agreement with the assumption made for defining dSCDs.

The trace gas absorption coefficient is calculated according to Eq. 2:

$$a_{gas} = \text{VMR} \cdot \xi_\lambda \cdot \rho \tag{2}$$

For the calculation of the depolarization ratio Δ, the main contributions are from N_2, CO_2, O_2 and Ar. Our implementation follows Bates (1984). Details are given in Appendix B. For the calculation of the Rayleigh cross-section Q_{Ray}, we follow the implementation of Goody and Yung (1989) (their equation 7.37), see also Platt et al. (2007) (their equation 19.5). The air scattering coefficient can then be calculated according to Eq. 3:

$$\sigma_{air} = Q_{Ray} \cdot \rho \tag{3}$$

and the Rayleigh scattering expansion coefficients β_l (e.g. Spurr et al., 2001), according to Eq. 4:

$$\beta_{air0} = 1, \beta_{air,1} = 0, \beta_{air,2} = (1 - \Delta)/(2 + \Delta). \tag{4}$$

4.2.2 Input for aerosols

The (*a priori*) aerosol data for total optical depth, average single scattering albedo ω and asymmetry parameter g (used to calculate the phase function moments) are time interpolated values from the co-located AERONET (Aerosol Robotic Network) station in Mexico City (V2, level 1.5 at http://aeronet.gsfc.nasa.gov). They are also extra-/interpolated at the retrieval wavelength. The *a priori* shape of the profile is taken from hourly averaged ceilometer data (García-Franco et al., 2018), interpolated at the middle layer height h of each layer.

The first part of MMF, the aerosol retrieval, is limited to the aerosol density profile and the total aerosol optical depth. The average single scattering albedo ω and asymmetry parameter g are not subject to retrieval and are assumed to be constant in all layers.

Fig. 3 (b) outlines the strategy how the aerosol contribution to the VLIDORT layer input parameters is calculated.

The hourly averages of (relative) aerosol density profiles in arbitrary units from ceilometer measurements between November 2009 to February 2013 are interpolated at measurement day time t and at retrieval grid middle heights h to provide a relative aerosol profile. This profile, turned into a partial optical depth per layer by multiplying with the layer thickness, is scaled to match the total aerosol extinction from AERONET τ_{aer}. The profile is then converted back into an intensive[3] quantity by division by layer thickness, usually known as aerosol extinction profile (extinction per unit length, AE). This is then used to calculate the aerosol scattering coefficient σ_{aer} in each layer by multiplying the layer aerosol extinction with the aerosol single scattering albedo ω_{aer}.

The aerosol absorption coefficient a_{aer} is the layer aerosol extinction times $(1-\omega_{\mathrm{aer}})$ and the aerosol phase function coefficients $\beta_{\mathrm{aer},l}$ can be calculated via the Henyey Greenstein phase function and the asymmetry parameter g, see Eq. 5, e.g. Hess et al. (1998), where l denotes the moment,

$$\beta_{\mathrm{aer},l} = (2l+1) \cdot g^l. \tag{5}$$

4.2.3 Calculating final VLIDORT input

As mentioned in the introduction to this section, the layer input parameters for VLIDORT are total optical depth τ and single scattering albedo ω in the layer, as well as the phase function coefficients β_l. The quantities which have been calculated so far are the aerosol and air contributions to β_l and the air and aerosol scattering coefficients σ_{air} and σ_{aer}, as well as the absorption coefficients a_{gas} from the trace gas in question and a_{aer} from the aerosol in each VLIDORT input layer (red boxes in Fig. 3). These quantities need to be combined to total layer input parameters.

The total layer optical depth is simply the product of the layer thickness and the sum of all extinction and scattering coefficients, see Eq. 6:

$$\tau = \Delta h \cdot (\sigma_{\mathrm{air}} + \sigma_{\mathrm{aer}} + a_{\mathrm{gas}} + a_{\mathrm{aer}}) \tag{6}$$

---

[3]bulk property that does not change when changing the size of the system

The combined single scattering albedo can be calculated as in Eq. 7:

$$\omega = (\sigma_{\text{air}} + \sigma_{\text{aer}}) \cdot \Delta h / \tau \tag{7}$$

The combined expansion coefficients are calculated as in Eq. 8:

$$\beta_l = (\beta_{\text{air,l}} \cdot \sigma_{\text{air}} + \beta_{\text{aer,l}} \cdot \sigma_{\text{aer}}) / (\sigma_{\text{air}} + \sigma_{\text{aer}}) \tag{8}$$

5 Since Jacobians with respect to changes of quantity χ in each layer are required, the normalized derivatives of the total primary optical quantities, τ, ω and β with respect to this quantity need to be supplied. In case of trace gas retrieval, $\chi = a_{\text{gas}}\Delta h$ and in case of aerosol retrieval, $\chi = \sigma_{\text{aer}}\Delta h + a_{\text{aer}}\Delta h$. Therefore, what needs to be done is to calculate the normalized derivatives of Eq. 6 – Eq. 8 with respect to these quantities. It should be remembered that β is a vector.

The three quantities for aerosol are calculated according to Eq. 9 to Eq. 11:

$$
10 \quad \frac{\chi}{\tau}\frac{d\tau}{d\chi} = \frac{(\sigma_{\text{aer}} + a_{\text{aer}})\Delta h}{\tau} \frac{d\tau}{d(\sigma_{\text{aer}} + a_{\text{aer}})\Delta h} = \frac{\sigma_{\text{aer}} + a_{\text{aer}}}{e} \tag{9}
$$

$$
\frac{\chi}{\omega}\frac{d\omega}{d\chi} = \frac{(\sigma_{\text{aer}} + a_{\text{aer}})\Delta h}{\omega} \cdot \left[\frac{\partial \omega}{\partial \sigma_{\text{aer}}}\frac{d\sigma_{\text{aer}}}{d[(\sigma_{\text{aer}} + a_{\text{aer}})\Delta h]} + \frac{\partial \omega}{\partial a_{\text{aer}}}\frac{da_{\text{aer}}}{d[(\sigma_{\text{aer}} + a_{\text{aer}})\Delta h]}\right]
$$

$$
= \frac{\sigma_{\text{aer}}a_{\text{gas}} - a_{\text{aer}}\sigma_{\text{air}}}{\omega e^2} \tag{10}
$$

$$
\frac{\chi}{\beta}\frac{d\beta}{d\chi} = \frac{(\sigma_{\text{aer}} + a_{\text{aer}})\Delta h}{\beta} \frac{d\beta}{d(\sigma_{\text{aer}} + a_{\text{aer}})\Delta h} = \frac{\sigma_{\text{aer}}}{\beta} \frac{\beta_{\text{aer}} - \beta}{\sigma_{\text{aer}} + \sigma_{\text{air}}} \tag{11}
$$

Here, e is the total extinction coefficient: $e = \tau / \Delta h$

15 For the trace gas Jacobian calculation, the corresponding normalized derivatives are according to Eq. 12 to Eq. 14

$$
\frac{\chi}{\tau}\frac{d\tau}{d\chi} = \frac{a_{\text{gas}}\Delta h}{\tau}\frac{d\tau}{da_{\text{gas}}} = \frac{a_{\text{gas}}}{e} \tag{12}
$$

$$
\frac{\chi}{\omega}\frac{d\omega}{d\chi} = \frac{a_{\text{gas}}\Delta h}{\omega}\frac{\omega}{a_{\text{gas}}} = -\frac{a_{\text{gas}}}{e} \tag{13}
$$

$$
\frac{\chi}{\beta}\frac{d\beta}{d\chi} = 0 \tag{14}
$$

4.3 Calculating dSCDs and weighting functions

20 The forward model outputs, intensities and intensity Jacobians, need to be converted into differential slant column densities and corresponding Jacobians. For each set of dSCD, we have to run the forward model 2 times: Once with the gas absorption included and once without the gas absorption. Each of these sets consists of simulations in the desired telescope directions and one simulation towards the zenith. Note that the output from VLIDORT is Kx, hence the immediate output from VLIDORT has to be divided by x in case of linear retrieval to give the Jacobian alone.

25 In the following, the intensity and Jacobian of the simulation towards the desired angles without gas absorption are denoted I_0^α and K_0^α, the intensity (Jacobian) with gas absorption towards the zenith I_g^z (K_g^z), the intensity (Jacobian) with gas absorption towards the desired angle I_g^α (K_g^α) and the intensity (Jacobian) without gas absorption towards the zenith I_0^z (K_0^z). The dSCD

can be calculated as in Eq. 15

$$\text{dSCD} = \ln\left(\frac{I_0^\alpha \cdot I_g^z}{I_g^\alpha \cdot I_0^z}\right)/\xi_\lambda \tag{15}$$

The corresponding weighting function K is calculated as in Eq.16:

$$K = \frac{\left(K_0^\alpha\, I_g^z\, I_g^\alpha\, I_0^z + I_0^\alpha\, K_g^z\, I_g^\alpha\, I_0^z - I_0^\alpha\, I_g^z\, K_g^\alpha\, I_0^z - I_0^\alpha\, I_g^z\, I_g^\alpha\, K_0^z\right)}{\left(I_0^\alpha\, I_g^z\, I_g^\alpha\, I_0^z\, \xi_\lambda\right)}. \tag{16}$$

5 Error analysis

The errors of gas profile retrievals in remote sensing applications can be divided into the following four different types: (Rodgers, 2000):

1. Smoothing error, arising from the constraint of the NO_2 and aerosol profiles,

2. Measurement noise error, arising from the noise in the spectra,

3. Parameter error, including different parameters as aerosol profiles and cross-sections, and the

4. Forward model error, that originates from the simplification and uncertainties in the radiative transfer algorithm:

The Gain matrix, as defined by Eq. 17, describes the change in retrieved x when measurement y changes. It can hence be used to map the uncertainty in measurement space to a state-vector uncertainty.

$$\text{Gain} := \frac{\partial x}{\partial y} = (K_i^T S_m^{-1} K_i + R)^{-1} K_i^T S_m \tag{17}$$

The error analysis in general produces an error pattern ϵ_y in the measurement space of vectors of the dSCDs retrieved by QDOAS and simulated by MMF. With help of the Gain matrix, this error pattern is then mapped as ϵ_x into the space of the solution state.

5.1 Smoothing error

The retrieved atmospheric state vector x only represents a smoothed version of the true real state. The partial column Averaging Kernel matrix AK_{pcol} describes how a change in the true atmospheric state vector x_{true} is translated into changes in the retrieved state vector x, according to Eq. 18:

$$x - x_a = AK_{pcol}(x_{true} - x_a) + \epsilon_x \tag{18}$$

The Averaging Kernel of partial column and total column (AK_{tot}) describe how the retrieved solution profile depends on the real atmosphere x_{true}. They have to be taken into account if the profile and the column is used. The part which is not explained by AK_{pcol} is explained by the retrieval error ϵ_x.

As MMF uses constrained least square fitting, the AK_{pcol} is calculated analytically by MMF itself for each scan according to Eq. 19:

$$AK_{pcol} := \underbrace{\frac{\partial x}{\partial x_{true}}}_{\text{definition}} = \underbrace{\text{Gain} \cdot \text{K}}_{\text{analytical calculation}} \tag{19}$$

The Averaging Kernel matrix is in general asymmetrical. The columns are representing response functions related to a per-turbation in a certain layer. The rows of the matrix represent the sensitivity of the NO_2 partial column of a certain layer (or concentration in a certain layer) to all the different true partial columns or concentrations.

If AK_{pcol} is expressed in units of partial columns (as here indicated by the subscript $_{pcol}$), the sum of the rows is the total column Averaging Kernel. It represents the sensitivity of the vertical column density (VCD) to the anomalies in different heights.

The change of Averaging Kernel under transformation of the units is expressed by two matrix multiplications: One by multiplying the diagonal matrix containing the partial air column in its diagonal $U_{aircols}$ from the right with the Averaging Kernel; the other by multiplying the inverse of the diagonal matrix $U_{aircols}^{-1}$ from the left side with the Averaging Kernel, see Eq. 20:

$$AK_{VMR} = U_{aircols}^{-1} \cdot AK_{pcol} \cdot U_{aircols} \tag{20}$$

The trace of the AK_{tot} matrix represents the DOF, the number of independent pieces of information in the profile retrieval, which is around 2 for the NO_2 retrieval.

Equation (18) separates the smoothing effect described with AK matrices from the others errors. Before comparing the retrieved profiles of MMF with profiles from models or other measurements, such as satellite measurements, it is necessary to smooth the profile from the other source with the AK from MMF (Rodgers and Connor, 2003). Alternatively, a smoothing error S_{smooth} for the profile can be calculated according to Rodgers (2000) from the *a priori* covariance matrix S_a and the Averaging Kernel. The latter is describing how the true atmospheric state varies, as a best estimate. Eq. 21 describes how sensitive the retrieved atmospheric state vector depends on the true atmospheric state:

$$AK = \frac{\partial x}{\partial x_{true}} \tag{21}$$

Both quantities can be given in different representations adjusted to the atmospheric state vector either as a fraction of the *a priori*, the VMR ($_{VMR}$), as number densities or partial column profiles ($_{pcol}$) as used above. Using AK_{VMR}, S_{smooth} can be calculated according to Eq. 22:

$$S_{smooth} = (AK_{VMR} - \mathbf{1})S_a, VMR(AK_{VMR} - \mathbf{1})^{\mathbf{T}} \tag{22}$$

The smoothing error for the VCD is then calculated from the full covariance matrix of the smoothing error S_{smooth} using a total column operator, see Eq. 23:

$$\sigma_{smooth} = \sqrt{\mathbf{g^T} \cdot \underbrace{(\mathrm{AK_{pcol}} - \mathbf{1})\mathrm{S_{a,pcol}}(\mathrm{AK_{pcol}} - \mathbf{1})^\mathbf{T}}_{\mathrm{S_{smooth}^{pcol}}} \cdot \mathbf{g}}, \tag{23}$$

where $\mathbf{g}$ is the total column operator for partial column profiles: $\mathbf{g^T} = (1, 1, 1, 1, 1, 1, 1, 1, 1,...1)$.

As described before, the NO$_2$ retrieval code uses a single *a priori* and covariance matrix taken from the chemical transport model WRF-Chem. This results in the sensitivities and smoothing errors represented in Fig. 4(a).

The aerosol retrieval, however, uses a Tikhonov constraint and no covariance matrix is available. The *a priori* for the aerosol extinction profile are reconstructed by the actual total aerosol optical depth reported by the daily AERONET measurements and the average vertical distribution, reconstructed from ceilometer measurements for each hour of the day. The covariance matrix for the aerosols $S_{a,aerosol}$ is obtained by assuming a 100% variability of the used *a priori* profile and an exponential correlation length of η =500 m between the different layers, as in the recent work by Wang et al. (2017), see Eq. 24:

$$S_{a,aerosol}[i,j] = (100\% \cdot \mathrm{AE_a[i]} \cdot \mathrm{AE_a[j]})\exp^{(-|z[i]-z[j]|/\eta)} \tag{24}$$

In the cases where no vertical aerosol extinction profile (AE-profile) retrieval is available because the retrieval failed, or no O_4 dSCDs were available in the first place, a NO$_2$ profile can still be retrieved by using the *a priori* AE-profile instead of the retrieved one. Since in that case, no information of the O$_4$ absorption is used, the estimated smoothing error S_{smooth} is then directly given by the *a priori* covariance matrix $S_{a,aerosol}$ for the AE-profile. The *a priori* information about the optical properties described by the aerosol extinction profile is designed for cloud free days and therefore the error analysis is just valid for such cloud free days.

We have assumed a constant sensitivity AK and a constant *a priori* covariance matrix S_a for the calculation. The AK of the trace gas profile indeed depends strongly on the aerosol profile. It also depends slightly on the trace gas profile itself. The S_a covariance matrix of the aerosol extinction profile should be given for each hour as the *a priori* profile varies with time of day. Therefore, the estimation of the smoothing error as it is calculated here, gives just a rough general idea about the size of the smoothing error.

5.2 Measurement noise

The measurement noise error can be calculated from the Gain matrix and the measurement noise matrix (S$_m$) (Rodgers, 2000). The diagonal Matrix (S$_m$) is already used in the optimal estimation of the profile retrieval to weight the different dSCDs of a scan according to the square of the errors from the QDOAS retrievals. The statistics of the measurement dSCDs errors and its dependence to the elevation angle has been presented in Fig. 2.

The measurement noise error matrix for both 1) the NO$_2$ profile and 2) aerosol extinction profile are calculated directly during the retrieval and are available from the MMF output of each measurement sequence as a full covariance matrix S_{noise},
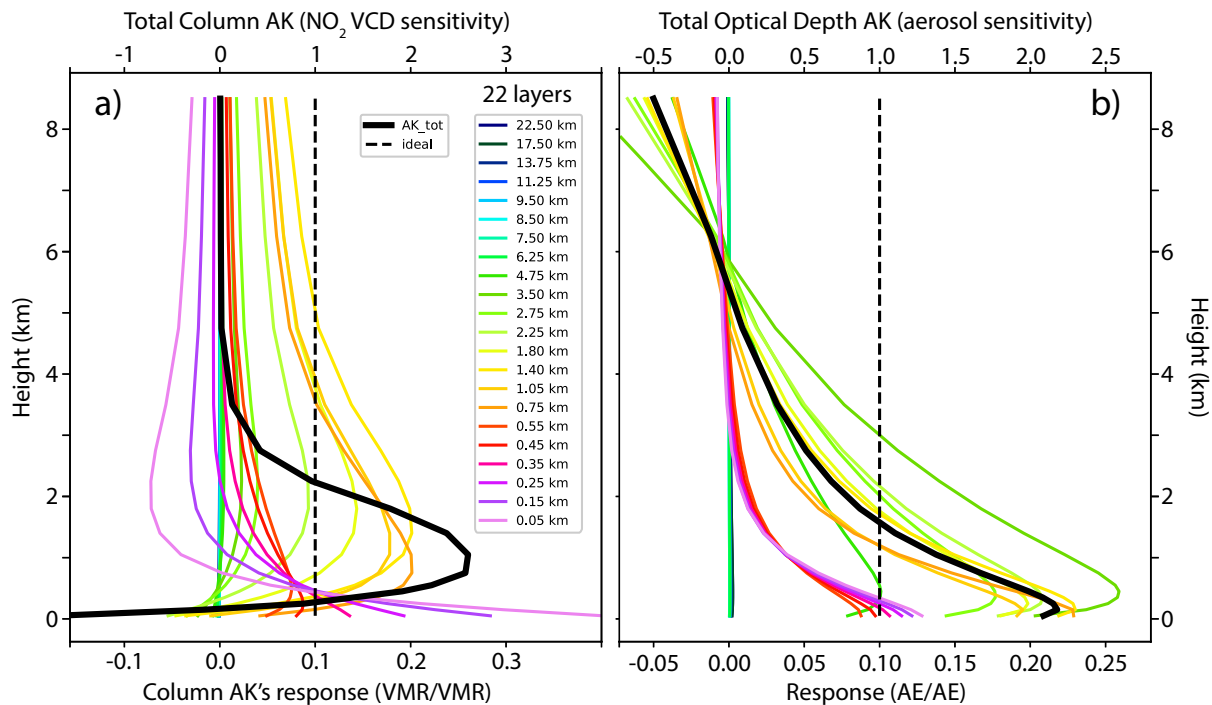
Figure 4. Averaging Kernel columns: (a, left) in VMR representation for NO_2 profile retrieval and (b, right) in the corresponding intensive quantity for the aerosol extinction (AE) profile. Each coloured line shows the expected response on perturbation in a certain layer and belongs to the lower axis. The total column Averaging Kernel: (a, left) for the NO_2-VCD and (b, right) for the total optical depth is given as a black line and belongs to the upper axis. The vertical dashed line in each panel indicate an ideal sensitivity of 1.0 in all altitudes.

given in units of partial columns and partial optical depths. The NO_2 total column error is then calculated from this and the total column operator, and amounts to around 2.4% of the VCD (see line 2 in Table 1). The errors in the profile are shown in Fig. 6.

5.3 Parameter errors

5 The parameter errors originate from all uncertainties in input-parameters in the forward model that are not properly fitted, such as the cross-sections and for the NO_2-profile retrieval also the used aerosol extinction profile.

5.3.1 Parameter error from Spectroscopy

The error originating from an uncertainty in the cross-section of 3% (Wang et al., 2017) is also around 3.0% in the vertical column (see line 3 in Table 1) and similar in the vertical profile. This error can be calculated using the generalized measurement

10 error covariance matrix $S_{spectroscopic}^{y}$ in the measurement space assuming that all retrieved dSCD are 3% too high (or low)

and using the outer product of the measurement state vector containing the retrieved dSCDs, see Eq. 25:

$$S^y_{spectroscopic} = (3.0\%)^2 \cdot yy^T \tag{25}$$

Using the Gain matrix, see Eq. 17, this can be translated into an error in the retrieval space, as demonstrated in Eq. 26:

$$S^x_{spectroscopic} = \mathrm{Gain} \cdot S^y_{spectroscopic} \cdot \mathrm{Gain}^T \tag{26}$$

5 From the $S^x_{spectroscopic}$ matrix, the error in the total column and profile is calculated as shown earlier in Sec.5.1. As expected, the error for the total column is 3% and the errors in the NO_2 VMR-profile are shown in Fig. 6. The spectroscopic error is a purely systematic error and affects all retrieval in the same manner.

5.3.2 Parameter error from aerosol profile

The AE-profile is crucial for the NO_2-profile retrieval because of its strong contribution to the airmass factor. The uncertainties
10 in this vector of input parameters arise from errors in the aerosol extinction profile retrieved from the spectral signature of the O_4-dimer. For the propagation of the error of the O_4-AE-retrieval into the NO_2-retrieval, we assume here that the total error in the AE-profile depends on just the two contributions: a) smoothing error and b) measurement noise errors.

The effect of the assumed aerosol content in each layer on the retrieved NO_2 profile is calculated by a sensitivity study. For this, 22 NO_2 retrievals are performed for the same measurement sequence (dSCDs) using slightly modified aerosol extinction
15 profiles. First, a normal retrieval with the best estimated aerosol extinction profile is retrieved. Then, the aerosol extinction profile is modified so that the partial extinction of the i-th layer is increased by 1% of the total optical depth with respect to the original aerosol extinction profile.

The difference between the perturbed and original NO_2 VMR profiles are combined into the matrix D, describing thus how the NO_2 VMR profile responds to changes in the aerosol at different heights. The result is presented in Fig. 5.
20 With the help of this matrix D_{VMR}, the different errors in the aerosol extinction profile, as measurement noise (see Sect. 5.2), smoothing error (see Sect. 5.1) or even due to the algorithm error according to Wang et al. (2017), can be propagated to the NO_2 profile and its VCD. The uncertainty in aerosol, represented by its $S_a, aerosol$ matrix, see Eq. 24, translates into an uncertainty in NO_2 VMR according to Eq. 27:

$$S^{aerosol}_{NO2-VMR} = D_{VMR} Sa_{aerosol} D_{VMR}{}^T \tag{27}$$

25 Using the technique from Eq. 23 with the unit transformation for the AK as in Eq. 20, this translates into and error on the VCD as in Eq. 28

$$error^{aerosol}_{NO2-VCD} = \sqrt{\mathbf{g^T} U_{aircols} \cdot D_{VMR} \cdot Sa_{aerosol} \cdot D_{VMR}{}^T U_{aircols} \cdot \mathbf{g}} \tag{28}$$

The propagation of the smoothing and measurement noise errors of the O_4 retrieval into the NO_2-retrieval (separately resulting in 4.6%, see line 6, and 2.2%, see line 5 in Table 1) results in a 5.1% error in the NO_2 VCD (see line 9 in Table 1). If
30 the algorithm error introduced by Wang et al. (2017) (7.8%, line 8 in Table 1) is included in the error propagated to NO_2, the
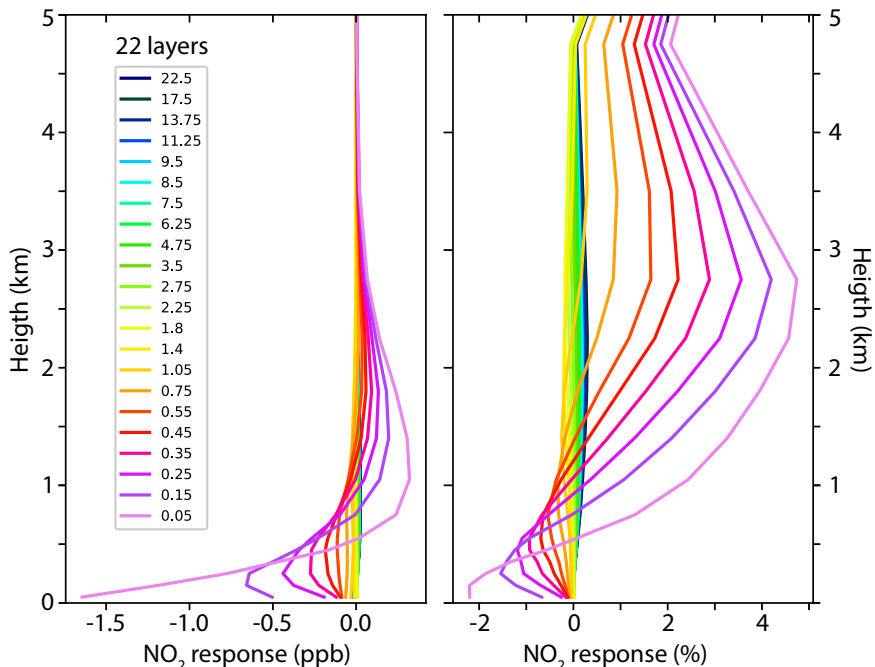
Figure 5. Plots showing the results of how sensitive the NO_2 profile is to changes in the aerosol extinction profile. Left: columns of the matrix D created to describe the response in the NO_2 VMR profile (the differences with respect to the original retrieval). Right: same as left but the response to the perturbation in the aerosol profile is given as fraction of the retrieved NO_2 profile.

error in NO_2 VCD is 9.3% (line 10 in Table 1). However the algorithm-error is calculated from the resulting residual of the fit and is dependent on the other error sources as mentioned earlier.

   If no O_4-retrieval is performed successfully, the aerosol *a priori* profile is used for the NO_2 retrieval. The error in this aerosol profile is estimated by its aforementioned assumed variability and S_a covariance matrix: A variability of 100% of the *a priori* profile is asumed for calculating the diagonal elements and an exponential correlation length of 500 m is used for calculating the off-axis elements of the S_a matrix. The error in the NO_2 VCD would be in this case 9.8% (see line 7 in Table 1)

5.4   Forward model error

The forward model error could be evaluated if an improved forward model was available. However, this is not the case. Errors in the forward model would result in systematic structures in the residual and a larger residual than expected from the error calculated by QDOAS for the slant columns. The least supported simplification in the forward model is the assumption of a horizontal homogeneity of gas and aerosols. A horizontal inhomogeneity leads to a set of slant columns in a scan which cannot be simulated by VLIDORT and the residuals of measured minus calculated slant columns indicate this error. Following Wang et al. (2017), we calculate the variance in the residuals as a function of viewing angle and hence the algorithm error. But as all
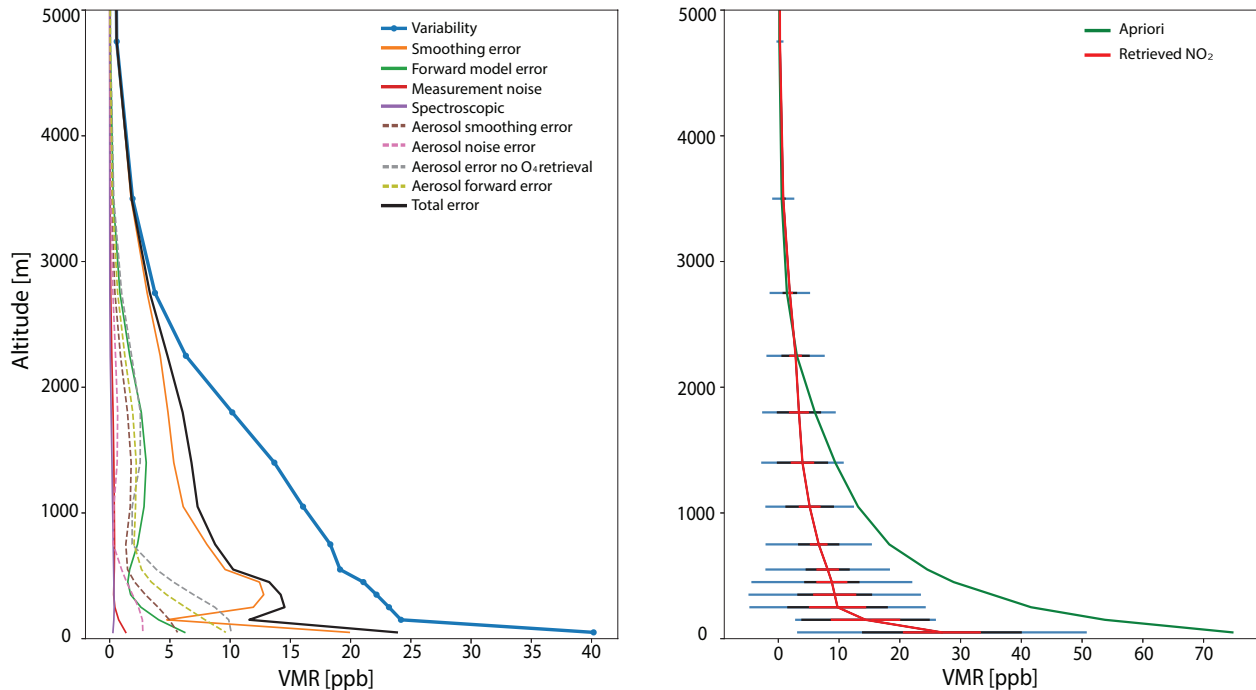
Figure 6. Altitude-dependent errors in a NO₂ VMR profile measured at 13:58 on May 20, 2016 (UTC-6h). a) The square root of the diagonal in the covariance matrix describing the individual error contributions in the VMR profile and b) the retrieved NO₂ VMR profile with corresponding error bars (total error and variability). The left panel also includes the *a priori* profile in green.

errors increase the residual the so called *algorithm error* is not identical to the forward model error. However, it is maybe a good way to check empirically if there are important error contributions missing in the analytical analysis.

5.5 Total error

The results from the error estimations are summarized in Table 1. The overall error in the NO₂ VCD is estimated to be around
5   14.1% (20.3% including the algorithm errors for NO₂ and O₄ calculated from the residuals). The contributions are 12.5% from smoothing, 2.4% from measurement noise, 3% from spectroscopy and 5.1 % from errors in the aerosol extinction profile. The algorithm error are 12.3% from the NO₂ retrieval itself and 7.8% from the O₄-AE retrieval. These errors are similar to those reported by Wang et al. (2017).

The error in the vertical column is smaller than the errors in the VMR profile for almost all layers (Fig. 6). This can be
10   explained by an anti-correlation in different partial column errors indicated by the full error covariance matrix. While the measurement noise seems to play a minor role, the smoothing and the aerosol profile are the main sources of error. Even

	Error	Description	$NO_2, \%$
1	Smoothing	Variability from model	12.6
2	Measurement noise	Fig. 2	2.4
3	Spectroscopy	3 %	3
4	from NO_2 residuals	20 residuals (diagonal)	(12.3)
5	Aerosol noise	from QDOAS	2.2
6	Aerosol smoothing	Wang et al.,(2017)	4.6
7	Aerosol variability	Wang et al.,(2017)	(9.8)
8	from O_4 residuals	20 residuals (diagonal)	(7.8)
9	Total aerosol	5,6	5.1
10	Total aerosol	5,6,8	9.3
11	Total, including	1,2,3,5,6	**14.1**
12	Total, including	1,2,3,7 (without O_4 retrieval)	16.4
13	Total error (all)	1,2,3,4,5,6,8	20.3

Table 1. Errors in NO_2 vertical column density as fraction of a retrieved VCD of 3.2×10^{16} molec./cm^2 measured at 13:58 on May 20 of 2016 (UTC-6h). The total error is calculated as the square root of the sum of squares of different independent errors. Different total errors are calculated: by including or not including the algorithm error (Wang et al., 2017); considering the two cases: that an aerosol extinction profile is retrieved from O_4-absorption or just an *a priori* guess is used. For the assumed variability of the aerosol extinction, the error due to the uncertainty remaining after an aerosol extinction profile retrieval is 5.1% instead of 9.8%. However, if the algorithm error according to Wang et al. (2017) is included, the remaining error due to the uncertainty in the aerosol profile is slightly better: 9.3% instead of the 9.8% without O_4 retrieval.

though the error might seem large, the retrievals still provide new and relevant information of NO_2 within the boundary layer of Mexico City.

6 Results

In this section, we present results of the NO_2 variability measured in one of the stations comprising the MAX-DOAS network operated in Mexico City, and compare them with *in situ* measurements performed at the surface. The location of the MAX-DOAS station, see Arellano et al. (2016) for a map, coincides with the aeronet station and the location of the surface sensor (19.32 N, 99.18 W). The launch location of the radio-sondes is close to the airport, around 15 km north-east from UNAM at 19.40 N, 99.20 W.

A data set from January 2015 to July 2016 (approx. 19 months) is considered in this study, in which both MAX-DOAS and *in situ* surface measurements were available. A total number of 2531 coincidences of hourly averages were found in this period, considering that at least 6 measurement sequences of the MAX-DOAS instrument in each reported hour needed to be available. The complete time series is presented in Fig. 7, showing hourly NO_2 averages of the *in situ* surface concentration in
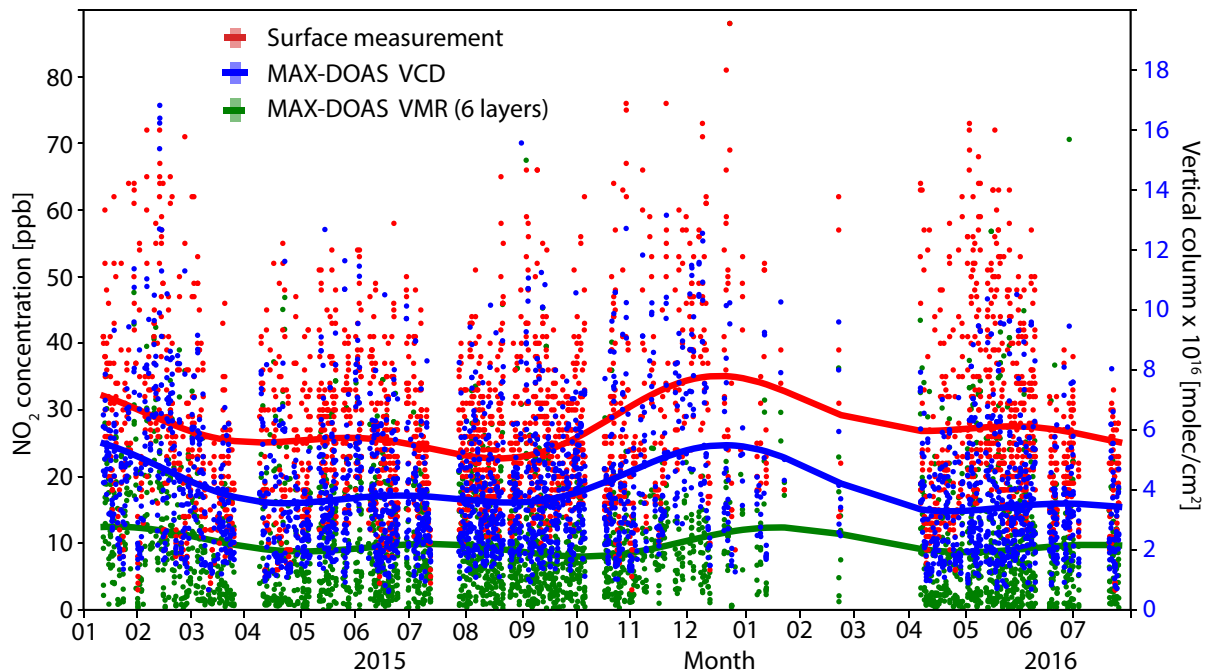
Figure 7. Hourly NO$_2$ averages of *in situ* surface concentrations (red) in ppb, total VCD's from the MAX-DOAS instrument (blue) in molecules/cm^2 and the average VMR of the first 6 layers (up to 550 m) in the retrieved MAX-DOAS profiles (green), also in ppb.

red, the total vertical column from the MAX-DOAS in blue, and the average VMR of its first 6 layers closest to the surface in green. This plot includes all MAX-DOAS results regardless of the sky conditions.

Apart from the large data gaps in the beginning of 2016, the time series is quite complete and the fitted annual periodic functions (a Fourier series constrained to a fixed seasonal cycle shape) applied to the three data sets show a similar pattern. VMR values from the surface measurements are clearly higher than the VMR's detected in the lowest layers of the MAX-DOAS retrievals.

The 2531 coincidences were correlated averaging different number of layers starting from the ground and the resulting Pearson's coefficients (*R*) are plotted in Fig. 8 (top). Currently, the integration times in the spectra from which the O$_4$ dSCDs are calculated, are not long enough to ensure an O$_4$ dSCD error resulting in DOF larger than 1 for the aerosol retrieval. Since we use a Tikhonov regularization for aerosol retrieval, this means that we can basically retrieve the total aerosol extinction. Due to the topographical circumstances in Mexico City, where the boundary layer rises steadily during the day, using an *a priori* that is calculated from hourly averages of ceilometer data will generally provide a good *a priori* profile shape. However, for days that likely have a very different aerosol profile from our *a priori* profile, the aerosol profile included in the trace gas forward model accounts for far more than the estimated error in 5.3.2 since this estimation uses a fixed percentage of the *a priori* profile in the S_a matrix. For cloudy days, for example, the form of the profile will look considerably different than the ceilometer averages. We are currently not able to retrieve such profiles. Hence, we limit our analysis to cloud free days. Currently, the
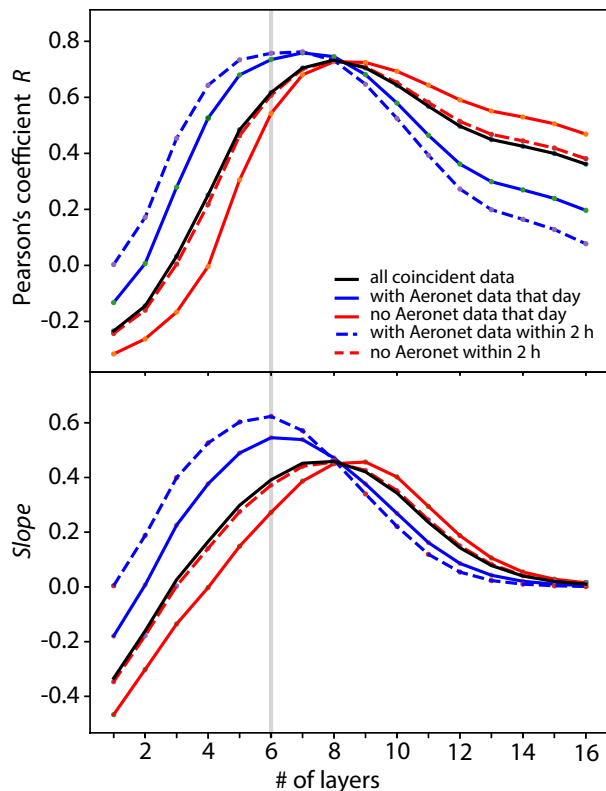
Figure 8. Pearson's correlation coefficients (top) obtained from hourly surface and MAX-DOAS coincident measurements as a function of the number of layers considered in the VMR averages. The slopes obtained from the linear regressions, performed forcing the intercept to be at zero to the same data sets, are shown in the lower panel. The layers below layer 6 are very likely inside the mixed boundary layer, while layers above layer 6 might be on the edge or above the boundary layer during some hours in the morning (García-Franco et al., 2018). The blue dashed lines only show data when AERONET data are avaible within 2 hours of the scan and hence limit the measurements to cloud free conditions. This selection criteria improves the correlation significantly.

retrieval chain has no cloud-screening algorithm included. As an ad-hoc solution, we use the presence of AERONET data on that day as an estimator for cloud free days. For our entire data set, for about half of the coincident measurements (1270) there was at least one AERONET measurement available on that particular day while for the rest of our data (1261), no AERONET data was available on that day.

5   Generally, a better correlation is found when averaged MAX-DOAS VMR's are compared to *in situ* surface measurements. Average R values larger than 0.7 are obtained in all cases when the first 6-8 layers are considered in the correlation. These correlations decrease rapidly when less layers are considered due to increased errors in the lowermost part of the profile. Naturally, the R value also decreases towards larger number of layers averaged since different air masses are measured at higher altitudes. As expected, slightly larger correlations are obtained for MAX-DOAS retrievals using a measured aerosol

10   input from the AERONET (blue traces in Fig. 8), which correspond to clear sky conditions.
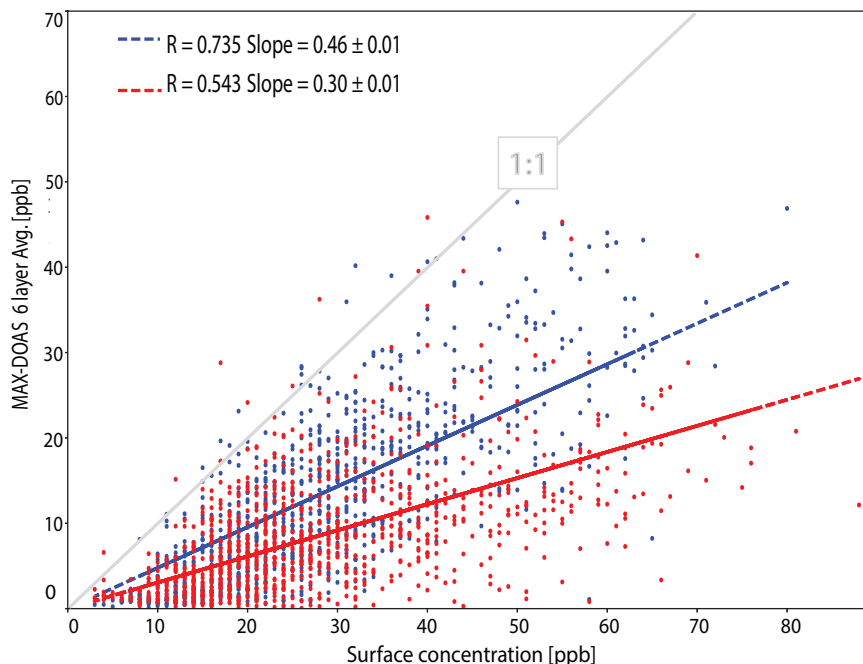
Figure 9. Correlation plot of the MAX-DOAS 6-layer VMR averages vs. the surface measurements shown separately for clear sky measurements in which aerosol data on that day was available (blue) and for MAX-DOAS retrievals with no AOD availability from AERONET, corresponding most likely to cloudy days (red).

Linear regressions as the ones shown in Fig. 9 were generated for each data set, in order to gain more information as to how the number of layers averaged relates to the VMR comparison with the *in situ* surface measurements. The slope of all coincident data using the first 7-8 layers is 0.45, and it can reach values above 0.6 considering the first 6 layers in clear sky conditions (AERONET data available within ± 1 h of the measurement time). We thus decide to use in this study the 6-layer VMR averages of our MAX-DOAS retrievals, reaching a height of 550 m above the ground level, in the comparisons we present with surface concentrations.

To investigate the difference in our data set between clear and cloudy days, a correlation plot is presented in Fig. 9 showing the linear regressions produced from the MAX-DOAS 6-layer VMR averages for the retrievals with AERONET availability on that day in blue and those retrievals using a default aerosol *a priori* in red. A significant improvement in the correlation coefficient going from 0.54 to 0.74 is evident in the plot. When all the coincident data is considered, regardless of if the retrieval had data available from the AERONET instrument on that day or not, the *R* and slope values are 0.62 and 0.39, respectively.

Examples of how the averaged 6-layer VMR's and VCD compare to the ground level concentrations in individual days are presented in Fig. 10. These examples were chosen to depict distinct diurnal patterns that occur in different times of the year. Again, the MAX-DOAS 6-layer product is consistently lower than the NO_2 concentrations measured at the surface. These,

together with the corresponding VCD's plotted on a different y-axis, follow the pattern of the surface measurements quite well. The MAX-DOAS instrument captures the features observed at the surface but not without some interesting differences.

May 4, 2016 was in the middle of a high pollution episode in Mexico City, in which a restriction on the use of private vehicles was declared during four days. Ozone had surpassed, at least in one of the stations from the monitoring network operated by the city government, the 165 ppb 1-hour average concentration. It is interesting to see in the May 4 plot, that indeed the surface concentrations of nitrogen dioxide were high in the morning, a condition favoring ozone production, but there is a large NO_2 peak just after noon in the MAX-DOAS VCD and 6-layer product data which is not detected at the surface. This is more evident from the individual measurements shown as dots than from the hour averages.

Other differences have to do with the evolution of the mixed layer height, which has been shown to have a rapid growth in the late morning, strongly influencing the surface concentrations (García-Franco et al., 2018). This is for example evident on the December 22 plot, where a peak is observed at 11 h and a second one at 14 h. This peak is strongest at 11 h in the case of the surface measurement, but the total column shows the peak at 14 h to be dominant. The mixed layer has grown in the mean time so that the registered 14 h surface concentration is lower despite there being more NO_2 molecules in the atmosphere.

In order to see the diurnal and seasonal patterns from both MAX-DOAS and surface measurements, all coincident measurements between January 2015 to July 2016 including days with clouds were averaged to a specific hour or month, respectively. For consistency, only the coincident 1-hour data was considered in order to make the data sets comparable. The mean diurnal evolution with standard deviations as vertical bars are shown in Fig. 11. The maxima of both surface and MAX-DOAS 6-layer products are at around 10 h, while that of the vertical column is shifted towards noon. This is expected from what is known from the emissions, growing mixed layer and ventilation patterns in Mexico City (e.g. García-Franco et al., 2018). Despite the fact that the offset in the curves for surface- and MAX-DOAS measurements appears to be nearly constant throughout the day, it would be interesting to investigate further how this offset varies in different seasons particularly when vertical mixing is not favoured.

Fig. 12, on the other hand, presents the compiled data considered in this study as monthly means in order to observe the seasonal variability and compare the data sets from these two measurement techniques. The three data products coincide in having the highest monthly mean values between April and June. A difference which is probably interesting to note is during December and January, when the concentrations from the surface measurements are relatively higher than those from the MAX-DOAS products. This might have to do with the fact that during these winter months the mixed layer is shallower than during the rest of the year, and the sensitivity of the MAX-DOAS instrument is reduced for the lowest layers as described above.

7 Conclusions

In this contribution we describe the methodology used to analyze the data produced by the network of MAX-DOAS instruments (Arellano et al., 2016) operating in the Mexico City Metropolitan Area. In general terms, MMF is a retrieval code developed to process the data acquired by the instruments converting the measured spectra together with other input parameters to vertical
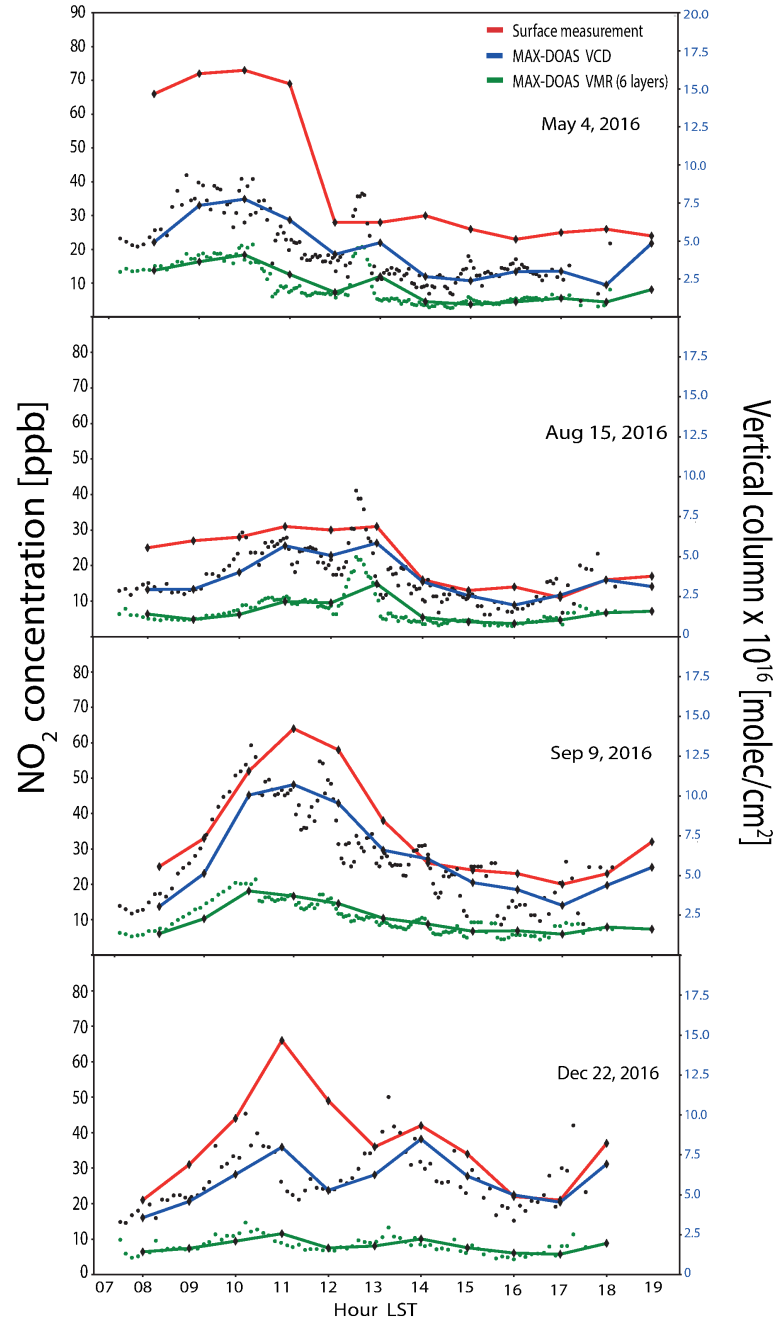
Figure 10. Example days showing the NO₂ variability in both VMR from the MAX-DOAS (green, < 550 m) and surface measurements (red), as well as the total vertical column densities (blue).
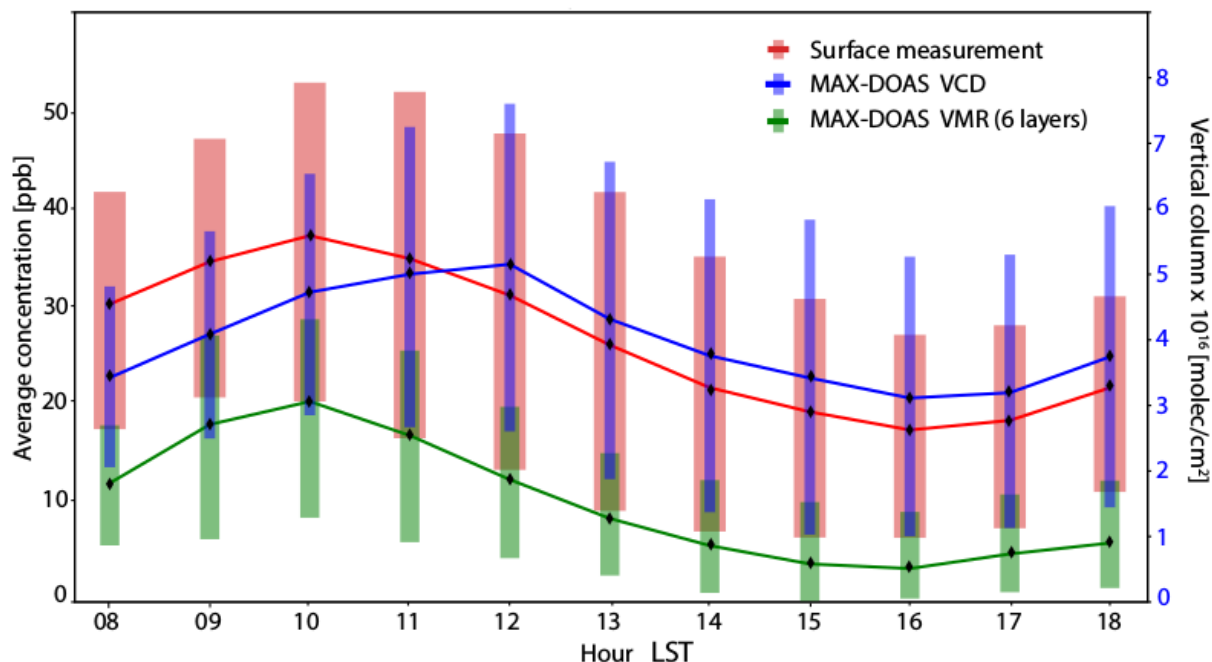
Figure 11. Diurnal NO_2 variability from hourly means of the entire data set spanning from January 2015 to July 2016. Only the data with coincident surface and MAX-DOAS measurements are included for consistency in the comparison. Vertical bars correspond to the standard deviations.

profiles of aerosols and certain trace gases. We have tested the performance of the code for NO_2 at one of the stations and present some diagnostics and a full error analysis of the results. In the case of NO_2, all error sources amount to about 14.1%, the smoothing error being the dominating one (12.5%) followed by the error due to the uncertainties in the aerosol extinction profile (5.1%).

5   Both the resulting total vertical column densities and a product consisting of the average VMR in the first 6 layers (< 550 m above the ground level), were compared to ground level NO_2 concentrations. Good correlations were obtained between the 6-layer product and the values from the surface measurements, with *R* values between 0.6 and 0.7. However, the MAX-DOAS systematically underestimates the ground level concentrations by a factor of about 0.6. This is consistent with the total column averaging kernels and variability Sa reported in Sect. 5.1, meaning that the MAX-DOAS instrument has a significantly lower

10   sensitivity near the surface and is most sensitive at a height of around 1 km. It is shown, however, that this underestimation is less for clear sky conditions as suggested from comparing data when aerosol optical depths where available from independent measurements.

Although results are shown only from one instrument located in the southern part of the city (UNAM), several years of data are available from three other stations at different locations within the metropolitan area (Acatlán, Vallejo and Cuautitlán)
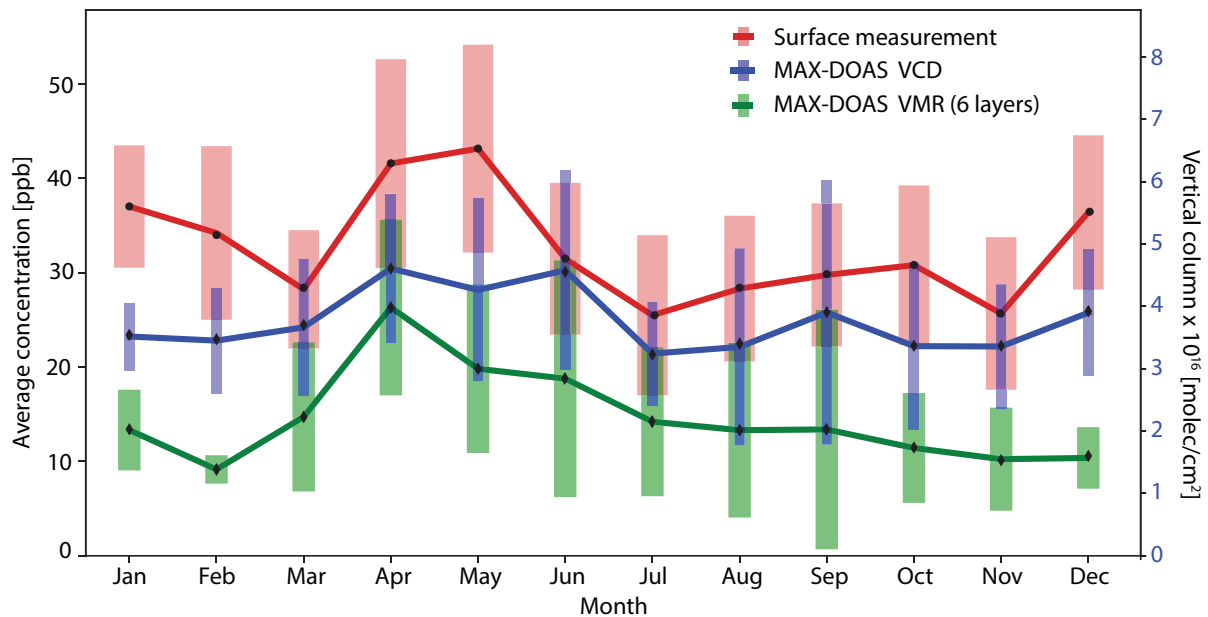
Figure 12. Annual NO$_2$ variability resulting from the monthly mean coincident data (surface and MAX-DOAS) between January 2015 and July 2016. The standard deviations are given in vertical bars.

that are being analyzed and used for studying the spatial and temporal variability of NO$_2$ in conjunction of several satellite products.

In this work we present a new and competitive retrieval code which has been developed for retrieving trace gas profiles from MAX-DOAS measurements. Since this study, it has been further improved to perform retrievals in logarithmic space to avoid unphysical negative partial columns and oscillations; it uses the more stable Levenberg-Marquardt iteration scheme and decouples the retrieval and simulation grids[4].

Further efforts include the improvement in the measurement noise by increasing the integration times during spectral acquisition. This will allow us to improve the retrieval of other gases such as formaldehyde (HCHO) and other weak absorbers. It will also enable us to use OE as retrieval strategy for aerosol retrieval and possibly increase the DOF to comparable values as for the NO$_2$ retrieval. This, together with an inclusion of a cloud-screening algorithm in the retrieval chain, will make the retrieval less dependent on the availability of AERONET data.

Appendix A

In a recent update of the code, implemented after the analysis presented here (i.e. not used for obtaining the results here), the retrieval space was changed from linear space to logarithmic retrieval space. This means that the retrieval works in a linear (dscd

---

[4]Details can be found in Appendix A

measurement)-logarithmic(profile retrieval) space now. This enhances the nonlinearity of the problem and requires a change of iteration scheme. The GN iteration scheme (Eq. 1) is replaced by a slightly slower but more stable Levenberg Marquardt (LM) iteration scheme, i.e. Eq. 1 is replaced by Eq. A1 for more non-linear inversion problems (Rodgers, 2000)

$$x_{i+1} = x_i + \left[(1+\gamma)R + K_i^T S_m^{-1} K_i\right]^{-1} \left[K_i^T S_m^{-1}(y - F(x_i)) - R(x_i - x_a)\right] \tag{A1}$$

5   The symbols mean the same as in Eq. 1: superscript T denotes transposed, superscript -1 denotes the inverse, subscript a indicates *a priori* values. S_m is the measurement error covariance matrix, y denotes the vector of measured differential slant column densities, $F(x_i)$ are the simulated differential slant column densities at iteration i, calculated using the forward model with input profile x_i, K_i is the Jacobian matrix at the i-th iteration.

    The new x_{i+1} in Eq. A1 is only accepted if the cost function in Eq. A2 decreases w.r.t the cost-function of the previous

10   iteration.

$$\mathrm{cost} = \sum_k^{\mathrm{angles}} \sum_j^{\mathrm{angles}} (\mathrm{y} - \mathrm{F(x)})_\mathrm{k} \mathrm{S_m^{-1}}^{\mathrm{kj}} (\mathrm{y} - \mathrm{F(x)})_\mathrm{j} + \sum_k^{\mathrm{layers}} \sum_j^{\mathrm{layers}} (\mathrm{x} - \mathrm{x_a})_\mathrm{k} \mathrm{Sa^{-1}}^{\mathrm{kj}} (\mathrm{x} - \mathrm{x_a})_\mathrm{j}. \tag{A2}$$

    If this is the case, x_{i+1} is accepted and if $(1+\gamma)$ is not yet equal to 1, the factor $(1+\gamma)$ is halved for the next iteration. If, however, the cost-function increases, the newly calculated x_{i+1} is discarded and the i-th calculation repeated with a factor $(1+\gamma)$ increased by a factor of 16.

15   In order to counteract the slowdown of the retrieval, more restrictions were placed on the observation geometry for a single scan: a single relative azimuth angle and a single solar zenith angle per scan. This means in particular that two different viewing directions cannot be treated as a single scan any longer. Also, it is no longer necessary to have the full simulation grid as the retrieval grid. The retrieval can be limited to the lower part of the simulation grid. Although the former change (w.r.t. observation geometry) means a significant cut in flexibility, it results in a retrieval time speed up of a factor of 4 and a more

20   typical retrieval time per scan and per constituent (i.e. for both aerosol and tracegas) is around 5 seconds.

    Tests using the logarithm of the partial layer vertical column density (for NO_2 retrieval) or layer extinction profile (for aerosol retrieval) motivated the change to the LM iteration scheme due to the increased non-linearity when working in a semi-log space as state-measurement space. With this new configuration, MMF has been participating in the Round-Robin comparison of different retrieval codes for the FRM4DOAS project (Frieß et al., 2018). It has also participated in the profile

25   retrieval from dSCD from the CINDI-2 campaign, both for NO_2 and HCHO (Tirpitz et al., in preparation).

    If the retrieval is to be performed in log-space, i.e. to work with $ln(x)$ instead of with x as the retrieval parameter, K in Eq. 16 is multiplied by x (Since the raw output from VLIDORT is Kx, no division by x is necessary, because the quantity needed in logarithmic space is Kx) and the uncertainty covariance matrix S_a in Eq. A1 needs to be left and right multiplied by $1/x$.

    The LM scheme of Eq. A1 has currently only been tested with OE and not with Tikhonov regularization, i.e. the aerosol

30   retrieval was also performed using OE.

Appendix B: Calculations for dry air density

In this appendix, we outline the calculation of Z, the molar mass of air M_a and the depolarization ratio Δ. We follow Ciddor (1996). If T is given in K (temperature in C is denoted as T_C), σ the wavenumber in $1/\mu$m, pressure P in Pa, volume mixing ratio of CO_2 in ppm, the constants in Eq. B1 - Eq. B14 have the following values:

$k_0 = 238.0185$	$a_0 = 1.58123 \times 10^{-6}$	$b_0 = 5.707 \times 10^{-6}$	$w_0 = 295.235$
$k_1 = 5792105.0$	$a_1 = -2.9331 \times 10^{-8}$	$b_1 = -2.051 \times 10^{-8}$	$w_1 = 2.6422$
$k_2 = 57.362$	$a_2 = 1.1043 \times 10^{-10}$	$c_0 = 1.9898 \times 10^{-4}$	$w_2 = -0.03238$
$k_3 = 167917.0$	$\alpha = 1.00062$	$c_1 = -2.376 \times 10^{-6}$	$w_3 = 0.004028$
$d = 1.83 \times 10^{-11}$	$\beta = 3.14 \times 10^{-8}$	$A = 1.2379 \times 10^{-5}$	$C = 33.937$
$e = -0.765 \times 10^{-8}$	$\gamma = 5.6 \times 10^{-7}$	$B = -1.912 \times 10^{-2}$	$D = -6.343 \times 10^{3}$

First, the saturation vapor pressure $\mathcal{S}$ is calculated according to Eq. B1 then the enhancement factor for water vapour in air, $\mathcal{F}$, is calculated according to Eq. B2 and with this, the molar fraction of water vapor in moist air x_w is calculated according to Eq.B3 where P_w is partial water vapor pressure in Pa.

$$\mathcal{S} = \exp\left(AT^2 + BT + C + D/T\right) \tag{B1}$$
$$\mathcal{F} = \alpha + \beta P + \gamma T_C^2 \tag{B2}$$
$$x_w = \mathcal{F} P_w / P \tag{B3}$$

The air density in dry air $n_{air,dry,450}$ (0 % humidity) at standard conditions (15 °C, 101.325 Pa, xCO_2 = 450 ppm) can be calculated as in Eq. B4 and from this, the dry air density at xCO_2 is calculated according to Eq. B5.

$$\left(n_{air,dry,450} - 1\right) \times 10^8 = \frac{k_1}{k_0 - \sigma^2} + \frac{k_3}{k_2 - \sigma^2} \tag{B4}$$
$$\left(n_{air,dry,xCO_2} - 1\right) = \left(n_{air,dry,450} - 1\right) \times 10^8 \left(1.0 + 0.534 \times 10^{-6} \cdot (xCO_2 - 450.0)\right) \tag{B5}$$

The equivalent quantity for water vapour, n_{wv}, is calculated as follows:

$$n_{wv} = 1.022 \cdot \left(w_0 + w_1 \sigma^2 + w_2 \sigma^4 + w_3 \sigma^6\right) \tag{B6}$$

The molar mass of dry air, M_a with xCO_2 is calculated as:

$$M_a = 10^{-3}\left(28.9635 + 12.011 \times 10^{-6}(xCO_2 - 400.0)\right) \tag{B7}$$

The compressibility of dry air, Z_a, and pure water vapour, Z_w, are calculated as:

$$Z_a = 1.0 - \frac{101325.0}{288.15}\left(a_0 + 15 a_1 + 225 a_2\right) \tag{B8}$$
$$Z_w = 1.0 - \frac{1333.0}{293.15}\left(a_0 + 20 a_1 + 400 a_2 + b_0 + 20 b_1 + c_0 + 20 c_1\right) + \left(\frac{1333.0}{293.15}\right)^2 (d + e) \tag{B9}$$

Table B1. depolarization ratios and VMR for main air constituents

gas	VMR/ppm	Δ gas
N_2	780840.0	see Eq. B16
O_2	209460.0	see Eq. B16
Ar	9340.0	0.0
CO_2	400.0	0.0814

Using Eq. B10 once with the values for Z, R and T for standard water vapour and once with the values for standard air, one can calculate ρ_{ws} and ρ_{axs}, respectively.

$$\rho = (pM_a/(ZR_{gas}T))(1 - x_w(1 - M_{mwv}/M_a)) \tag{B10}$$

Here, $R_{gas} = 8.3144621$ J/mol/K is the gas constant, $M_{mwv} = 0.018015$ kg/mol is the molar mass of water vapour. Z, the compressibility of moist air at T, x_w and P can be calculated as

$$Z = 1.0 - (P/T)(a_0 + a_1 T_C + a_2 T_C^2 + (b_0 + b_1 T_C)x_w + (c_0 + c_1 T_C)x_w^2) + (P/T)^2 (d + e\,x_w^2) \tag{B11}$$

Using again Eq. B10, with the actual values for P, x_w and Z, the density of the dry air component can be calculated according to Eq. B12 and the density of the water vapour component can be calculated according to Eq. B13

$$\rho_{\text{dry air}} = P M_a (1 - x_w)/(Z R_{gas} T) \tag{B12}$$

$$\rho_{wv} = P M_{mwv} x_w/(Z R_{gas} T) \tag{B13}$$

Finally, the number density of the air ρ and the refractive index n are calculated as:

$$\rho = \frac{\rho_{\text{dry air}}}{M_a} A_v \tag{B14}$$

$$n = \frac{\rho_{\text{dry air}}}{\rho_{axs}} (n_{\text{air,dry,xCO}_2} - 1) + \frac{\rho_{wv}}{\rho_{ws}} (n_{wv} - 1) \tag{B15}$$

Here, $A_v = 6.02214129 \times 10^{23}$ is the Avogadro number.

We use the N_2, O_2 and CO_2 depolarization factors from Bates (1984) and fixed VMR as summarized in Table B1 and calculate the wavelength dependent depolarization factor via Eq. B16 where F is the so called King factor and is calculated for N_2 (λ in μm) and O_2 according to Eq. B18 and Eq. B19, respectively. The complete depolarization factor is then calculated according to Eq. B19

$$\Delta = 6.0 \cdot (1 - F)/(-7F - 3) \tag{B16}$$

$$F(N_2) = 1.034 + 3.17 \times 10^{-4}/\lambda^2 \tag{B17}$$

$$F(O_2) = 1.096 + 1.385 \times 10^{-3}/\lambda^2 + 1.448 \times 10^{-4}/\lambda^4 \tag{B18}$$

$$\Delta = \sum (\Delta_i \text{VMR}_i), \quad i = N_2, O_2, Ar, CO_2 \tag{B19}$$

For the Rayleigh scattering cross section, we implement equation 7.37 from Goody and Yung (1989) and equation 19.5 from Platt et al. (2007), see Eq. B20.

$$Q_{\text{Ray}} = \frac{24\pi^3(n^2-1)^2}{\lambda^4 \rho^2 (n^2+2)^2} \frac{6+3\Delta}{6-7\Delta} \tag{B20}$$

Author contributions. MMF: part of Abstract and Sect. 1, Fig. 1, Fig. 2, Fig. 3, Sect. 4, Appendix A and B, retrieval code development and testing, retrieval chain setup from spectra to profiles, retrieval parameter choice for MMF, software support CR: parts of Sect. 2, Sect. 3. QDOAS setup, dSCD retrieval parameter choice, technical support WS and ZO: parts of Abstract, Sect. 5, Fig. 4 – 12, part of Sect. 6 and 7. Data retrieval, data analysis and interpretation, sensitivity tests and complete error analysis. JA: Sect. 2, instrument construction, installation and maintenance AB: parts of Sect. 2, technical support and data management support, instrument maintenance JAGR: part of Sect. 4.2.1, WRF-Chem simulations that serve as a-priori data for NO_2 retrieval MG: Sect. 1, Sect 6 and Sect. 7., data analysis and interpretation.

Competing interests. The authors declare that they have no conflict of interest

Acknowledgements. We would like to thank the financial support provided by CONACYT (grants 275239 & 290589) and DGAPA-UNAM (grants IN107417,IN111418 and IA100716 & M.M. Friedrich's postdoctoral fellowship). SEDEMA is acknowledged for providing the *in situ* surface concentrations from their monitoring network (RAMA) as well for partially supporting the MAX-DOAS network, and A. Krueger, A. Rodríguez, H. Soto and D. Flores are thanked for their technical assistance. We thank C. Fayt (caroline.fayt@aeronomie.be) and M. Van Roozendael (michelv@aeronomie.be) and Thomas Danckaert for the free use of the QDOAS software and we thank R. Spurr for free use of the VLIDORT radiative transfer code package. We thank the Solarimetric Mexican Service for their effort in establishing and maintaining the AERONET Mexico City site. We thank the University of Wyoming Department of Atmospheric Science for providing the sounding data on http://weather.uwyo.edu/upperair/sounding.html.

References

Arellano, J., Krüger, A., Rivera, C., Stremme, W., Friedrich, M., Bezanilla, A., and Grutter, M.: The MAX-DOAS network in Mexico City to measure atmospheric pollutants, Atmosfera, 29, 157–167, http://www.revistascca.unam.mx/atm/index.php/atm/article/view/ATM.2016.29.02.05, 2016.

5 Bates, D. R.: Rayleigh scattering by air, Planet. Space Sci., 32, 785–790, https://doi.org/10.1016/0032-0633(84)90102-8, 1984.

Buchwitz, M., Rozanov, V. V., and Burrows, J. P.: Development of a correlated-k distribution band model scheme for the radiative transfer program GOMETRAN/SCIATRAN for retrieval of atmospheric constituents from SCIMACHY/ENVISAT-1 data, in: Satellite Remote Sensing of Clouds and the Atmosphere III, vol. 3495 of Proc. SPIE, pp. 171–186, https://doi.org/10.1117/12.332681, 1998.

Burrows, J. P., Richter, A., Dehn, A., Deters, B., Himmelmann, S., Voigt, S., and Orphal, J.: Atmospheric remote-sensing reference data
10 from GOME. 2. Temperature dependent absorption cross sections of O_3 in the 231-794 nm range., J. Quant. Spec. Radiat. Transf., 61, 509–517, https://doi.org/10.1016/S0022-4073(98)00037-5, 1999.

Carlson, D., Donohoue, D., Platt, U., and Simpson, W. R.: A low power automated MAX-DOAS instrument for the Arctic and other remote unmanned locations, Atmospheric Measurement Techniques, 3, 429–439, 2010.

Ciddor, P. E.: Refractive index of air: new equations for the visible and near infrared, Appl. Opt., 35, 1566,
15 https://doi.org/10.1364/AO.35.001566, 1996.

Coburn, S., Dix, B., Sinreich, R., and Volkamer, R.: The CU ground MAX-DOAS instrument: characterization of RMS noise limitations and first measurements near Pensacola, FL of BrO, IO, and CHOCHO, Atmospheric Measurement Techniques, 4, 2421–2439, https://doi.org/10.5194/amt-4-2421-2011, 2011.

Dahlback, A. and Stamnes, K.: A new spherical model for computing the radiation field available for photolysis and heating at twilight,
20 Planetary Space Science, 39, 671–683, https://doi.org/10.1016/0032-0633(91)90061-E, 1991.

Danckaert, T., Fayt, C., Van Roozendael, M., De Smedt, I., Letocart, V., Merlaud, A., and Pinardi, G.: QDOAS Software user manual, Belgian Institute for Space Aeronomy, 2013.

Finlayson-Pitts, B. J. and Pitts, J. N.: Chemistry of the upper and lower atmosphere: theory, experiments, and applications, Academic Press, San Diego, CA, 2000.

25 Frieß, U., Monks, P. S., Remedios, J. J., Rozanov, A., Sinreich, R., Wagner, T., and Platt, U.: MAX-DOAS O_4 measurements: A new technique to derive information on atmospheric aerosols: 2. Modeling studies, Journal of Geophysical Research (Atmospheres), 111, D14203, https://doi.org/10.1029/2005JD006618, 2006.

Frieß, U., Beirle, S., Alvarado Bonilla, L., Bösch, T., Friedrich, M. M., Hendrick, F., Piters, A., Richter, A., van Roozendael, M., Rozanov, V. V., Spinei, E., Tirpitz, J.-L., Vlemmix, T., Wagner, T., and Wang, Y.: Intercomparison of MAX-DOAS Vertical Profile Retrieval Algo-
30 rithms: Studies using Synthetic Data, Atmospheric Measurement Techniques Discussions, 2018, 1–40, https://doi.org/10.5194/amt-2018-423, 2018.

Galle, B., Johansson, M., Rivera, C., Zhang, Y., Kihlman, M., Kern, C., Lehmann, T., Platt, U., Arellano, S., and Hidalgo, S.: Network for Observation of Volcanic and Atmospheric Change (NOVAC) A global network for volcanic gas monitoring: Network layout and instrument description, Journal of Geophysical Research, 115, D05 304, https://doi.org/10.1029/2009JD011823, 2010.

35 García-Franco, J., Stremme, W., Bezanilla, A., Ruiz-Angulo, A., and Grutter, M.: Variability of the Mixed-Layer Height Over Mexico City, Boundary-Layer Meteorol., https://doi.org/10.1007/s10546-018-0334-x, 2018.

Goody, R. M. and Yung, Y. L.: Atmospheric radiation : theoretical basis, 1989.

Hendrick, F., Müller, J.-F., Clémer, K., Wang, P., De Mazière, M., Fayt, C., Gielen, C., Hermans, C., Ma, J. Z., Pinardi, G., Stavrakou, T., Vlemmix, T., and Van Roozendael, M.: Four years of ground-based MAX-DOAS observations of HONO and NO_2 in the Beijing area, Atmospheric Chemistry and Physics, 14, 765–781, https://doi.org/10.5194/acp-14-765-2014, 2014.

Hermans, C., Vandaele, A. C., Carleer, M., Fally, S., Colin, R., Jenouvrier, A., Coquart, B., and Mérienne, M. F.: Absorption cross-sections of atmospheric constituents: NO_2, O_2, and H_2O, Environmental Science and Pollution Research, 6, 151–158, 1999.

Hess, M., Koepke, P., and Schult, I.: Optical Properties of Aerosols and Clouds: The Software Package OPAC., Bulletin of the American Meteorological Society, 79, 831–844, https://doi.org/10.1175/1520-0477(1998)079<0831:OPOAAC>2.0.CO;2, 1998.

Hönninger, G., Bobrowski, N., Palenque, E. R., Torrez, R., and Platt, U.: Reactive bromine and sulfur emissions at Salar de Uyuni, Bolivia, Journal Geophysical Research Letters, 31, L04101, https://doi.org/10.1029/2003GL018818, 2004.

Johansson, M., Rivera, C., de Foy, B., Lei, W., Song, J., Zhang, Y., Galle, B., and Molina, L.: Mobile mini-DOAS measurement of the outflow of NO_2 and HCHO from Mexico City, Atmospheric Chemistry and Physics, 9, 5647–5653, https://doi.org/10.5194/acp-9-5647-2009, 2009.

Kirmse, B., Delon, A., and Jost, R.: NO_2 absorption cross section and its temperature dependence, J. Geophys. Res., 102, 16, https://doi.org/10.1029/97JD00075, 1997.

Kurucz, R. L., Furenlid, I., Brault, J., and Testerman, L.: Solar flux atlas from 296 nm to 1300 nm, National Solar Observatory Atlas No. 1, 1984.

Marquard, L.: Modellierung des Strahlungstransports in der Erdatmosphäre für absorptionsspektroskopische Messungen im ultravioletten und sichtbaren Spektralbereich, http://books.google.se/books?id=1hm8cQAACAAJ, 1998.

Marquard, L. C., Wagner, T., and Platt, U.: Improved air mass factor concepts for scattered radiation differential optical absorption spectroscopy of atmospheric species, Journal of Geophysics Research, 105, 1315–1327, https://doi.org/10.1029/1999JD900340, 2000.

Melamed, M. L., Basaldud, R., Steinbrecher, R., Emeis, S., Ruíz-Suárez, L. G., and Grutter, M.: Detection of pollution transport events southeast of Mexico City using ground-based visible spectroscopy measurements of nitrogen dioxide, Atmospheric Chemistry and Physics, 9, 4827–4840, https://doi.org/10.5194/acp-9-4827-2009, 2009.

Meller, R. and Moortgat, G. K.: Temperature dependence of the absorption cross sections of formaldehyde between 223 K and 323 K in the wavelength range 225-375 nm, Journal of Geophysical Research, 105, 7089–7101, 2000.

Molina, L. T. and Molina, M. J.: Air quality in the Mexico megacity : an integrated assessment, Kluwer Academic Publishers, Dordrecht; Boston, 2002.

Orphal, J.: A critical review of the absorption cross-sections of O_3 and NO_2 in the ultraviolet and visible, JPPA, 157, 185–209, https://doi.org/10.1016/S1010-6030(03)00061-3, 2002.

Ortega, I., Koenig, T., Sinreich, R., Thomson, D., and Volkamer, R.: The CU 2-D-MAX-DOAS instrument - Part 1: Retrieval of 3-D distributions of NO_2 and azimuth-dependent OVOC ratios, Atmospheric Measurement Techniques, 8, 2371–2395, https://doi.org/10.5194/amt-8-2371-2015, 2015.

Palazzi, E., Petritoli, A., Giovanelli, G., Kostadinov, I., Bortoli, D., Ravegnani, F., and Sackey, S. S.: PROMSAR: A backward Monte Carlo spherical RTM for the analysis of DOAS remote sensing measurements, Advances in Space Research, 36, 1007–1014, https://doi.org/10.1016/j.asr.2005.05.017, 2005.

Perliski, L. M. and Solomon, S.: On the evaluation of air mass factors for atmospheric near-ultraviolet and visible absorption spectroscopy, Journal of Geophysics Research, 98, 10 363, https://doi.org/10.1029/93JD00465, 1993.

Platt, U. and Stutz, J.: Differential Optical Absorption Spectroscopy, Springer-Verlag Berlin Heidelberg, https://doi.org/10.1007/978-3-540-75776-4, 2008.

Platt, U., Pfeilsticker, K., and Vollmer, M.: Radiation and Optics in the Atmosphere, p. 1165, https://doi.org/10.1007/978-0-387-30420-5_19, 2007.

5   Rahpoe, N., von Savigny, C., Weber, M., Rozanov, A. V., Bovensmann, H., and Burrows, J. P.: Error budget analysis of SCIAMACHY limb ozone profile retrievals using the SCIATRAN model, Atmospheric Measurement Techniques, 6, 2825–2837, https://doi.org/10.5194/amt-6-2825-2013, 2013a.

Rahpoe, N., von Savigny, C., Weber, M., Rozanov, A. V., Bovensmann, H., and Burrows, J. P.: Error budget analysis of SCIA-MACHY limb ozone profile retrievals using the SCIATRAN model, Atmospheric Measurement Techniques Discussions, 6, 4645–4676,

10   https://doi.org/10.5194/amtd-6-4645-2013, 2013b.

Rivera, C., Barrera, H., Grutter, M., Zavala, M., Galle, B., Bei, N., Li, G., and Molina, L. T.: NO_2 fluxes from Tijuana using a mobile mini-DOAS during Cal-Mex 2010, Atmospheric Environment, 70, 532–539, https://doi.org/10.1016/j.atmosenv.2012.12.026, 2013.

Rodgers, C. D.: Inverse Methods for Atmospheric Sounding: Theory and Practice, World Scientific Publishing Co, https://doi.org/10.1142/3171, 2000.

15   Rodgers, C. D. and Connor, B. J.: Intercomparison of remote sounding instruments, Journal of Geophysical Research (Atmospheres), 108, 4116, https://doi.org/10.1029/2002JD002299, 2003.

Rozanov, V. V., Rozanov, A. V., Kokhanovsky, A. A., and Burrows, J. P.: Radiative transfer through terrestrial atmosphere and ocean: Software package SCIATRAN, J. Quant. Spec. Radiat. Transf., 133, 13–71, https://doi.org/10.1016/j.jqsrt.2013.07.004, 2014.

Rozanov, V. V., Dinter, T., Rozanov, A. V., Wolanin, A., Bracher, A., and Burrows, J. P.: Radiative transfer modeling through terrestrial

20   atmosphere and ocean accounting for inelastic processes: Software package SCIATRAN, J. Quant. Spec. Radiat. Transf., 194, 65–85, https://doi.org/10.1016/j.jqsrt.2017.03.009, 2017.

Spurr, R.: VLIDORT: A linearized pseudo-spherical vector discrete ordinate radiative transfer code for forward model and retrieval studies in multilayer multiple scattering media, Journal of Quantitative Spectroscopy & Radiative Transfer, pp. 316–342, 2006.

Spurr, R.: User's Guide VLIDORT Version 2.6, RT Solutions, Inc., 2013.

25   Spurr, R. J. D., Kurosu, T. P., and Chance, K. V.: A linearized discrete ordinate radiative transfer model for atmospheric remote-sensing retrieval, Journal of Quantitative Spectroscopy and Radiative Transfer, 68, 689–735, https://doi.org/10.1016/S0022-4073(00)00055-8, 2001.

Stamnes, K., Tsay, S.-C., Jayaweera, K., and Wiscombe, W.: Numerically stable algorithm for discrete-ordinate-method radiative transfer in multiple scattering and emitting layered media, Applied Optics, 27, 2502–2509, https://doi.org/10.1364/AO.27.002502, 1988.

30   Steck, T.: Methods for determining regularization for atmospheric retrieval problems, Appl. Opt., 41, 1788–1797, https://doi.org/10.1364/AO.41.001788, 2002.

Tirpitz, J.-L., Frieß, U., Hendrick, F., Alberti, C., Allaart, M., Apituley, A., Bais, A., Beirle, S., Benavent, N., Berkhout, S., Bösch, T., Bognar, K., Bruchkouski, I., Chan, K. L., Chengxin, Z., den Hoed, M., Donner, S., Drosoglou, T., Friedrich, M. M., Frumau, A., Gast, L., Gomez, L., Gielen, C., Hao, N., Hensen, A., Henzing, B., Hoque, S., Irie, H., Jin, J., Koenig, T. K., Kreher, K., Kuhn, J., Kumar, V., Lampel,

35   J., Li, A., Liu, C., Ma, J., Merlaud, A., Mishra, A., Nieto, D., Peters, E., Pinardi, G., Piters, A., Pöhler, D., Postylyakov, O., Richter, A., van Roozendael, M., Schmitt, S., Sinha, V., Spinei, E., Stein, D., Swart, D., Tack, F., Vlemmix, T., van der Hoff, R., Vonk, J., Wagner, T., Wang, S., Wang, Y., Wang, Z., Wenig, M., Wiegner, M., Wittrock, F., Xie, P., Xing, C., Xu, J., and Zhao, X.: DOAS Vertical Profile Retrieval Algorithms: Studies on Field Data from the CINDI-2 Campaign, Atmospheric Measurement Techniques, in preparation.

Vandaele, A. C., Hermans, C., Simon, P. C., Carleer, M., Colin, R., Fally, S., Mérienne, M. F., Jenouvrier, A., and Coquart, B.: Measurements of the NO_2 absorption cross-section from 42 000 cm^{-1} to 10 000 cm^{-1} (238-1000 nm) at 220 K and 294 K, Journal of Quantitative Spectroscopy and Radiative Transfer, 59, 171–184, 1998.

Vandaele, A. C., Hermans, C., Fally, S., Carleer, M., Merienne, M.-F., Jenouvrier, A., Coquart, B., and Colin, R.: Absorption cross-sections of NO_2: simulation of temperature and pressure effects, J. Quant. Spec. Radiat. Transf., 76, 373–391, https://doi.org/10.1016/S0022-4073(02)00064-X, 2003.

Vidot, J., Jourdan, O., Kokhanosvky, A. A., Szczap, F., Giraud, V., and Rozanov, V. V.: Retrieval of tropospheric NO_2 columns from satellite measurements in presence of cirrus: A theoretical sensitivity study using SCIATRAN and prospect application for the A-Train, J. Quant. Spec. Radiat. Transf., 111, 586–601, 2010.

von Friedeburg, C.: Derivation of Trace Gas Information combining Differential Optical Absorption Spectroscopy with Radiative Transfer Modelling, Ph.D. thesis, Ruperto-Carola University of Heidelberg, Germany (1993), 2003.

von Friedeburg, C., Wagner, T., Geyer, A., Kaiser, N., Vogel, B., Vogel, H., and Platt, U.: Derivation of tropospheric NO_3 profiles using off-axis differential optical absorption spectroscopy measurements during sunrise and comparison with simulations, Journal of Geophysical Research (Atmospheres), 107, 4168, https://doi.org/10.1029/2001JD000481, 2002.

Wagner, T., Beirle, S., Brauers, T., Deutschmann, T., Frieß, U., Hak, C., Halla, J. D., Heue, K. P., Junkermann, W., Li, X., Platt, U., and Pundt-Gruber, I.: Inversion of tropospheric profiles of aerosol extinction and HCHO and NO_2 mixing ratios from MAX-DOAS observations in Milano during the summer of 2003 and comparison with independent data sets, Atmospheric Measurement Techniques, 4, 2685–2715, https://doi.org/10.5194/amt-4-2685-2011, 2011.

Wang, S., Cuevas, C. A., Frieß, U., and Saiz-Lopez, A.: MAX-DOAS retrieval of aerosol extinction properties in Madrid, Spain, Atmospheric Measurement Techniques, 9, 5089–5101, https://doi.org/10.5194/amt-9-5089-2016, 2016.

Wang, Y., Lampel, J., Xie, P., Beirle, S., Li, A., Wu, D., and Wagner, T.: Ground-based MAX-DOAS observations of tropospheric aerosols, NO_2, SO_2 and HCHO in Wuxi, China, from 2011 to 2014, Atmospheric Chemistry and Physics, 17, 2189–2215, https://doi.org/10.5194/acp-17-2189-2017, 2017.

Wilmouth, D. M., Hanisco, T. F., Donaue, N. M., and Anderson, J. G.: Fourier Transform Ultraviolet Spectroscopy of the $A^2\prod_{3/2} \leftarrow X^2\prod_{3/2}$, Journal of Physical Chemistry A, 103, 8935–8945, 1999.

Wittrock, F., Oetjen, H., Richter, A., Fietkau, S., Medeke, T., Rozanov, A., and Burrows, J. P.: MAX-DOAS measurements of atmospheric trace gases in Ny-Ålesund - Radiative transfer studies and their application, Atmospheric Chemistry and Physics, 4, 955–966, https://doi.org/10.5194/acp-4-955-2004, 2004.